POLITECNICO DI TORINO - EPFL - GRENOBLE INP PHELMA

Master Degree course in Micro- and Nanotechnologies for Integrated Systems

Master Thesis

Design and Implementation of a Second Harmonic Generation Microscope: Exploring Ferroelectric Domain Poling in LiNbO$_3$

Prof. Amir SAFAVI-NAEINI
Prof. Enzo Mario DI FABRIZIO
Alex HWANG, Hubert STOKOWSKI

Candidate
Andrea CERCACI

ACADEMIC YEAR 2022-2023

Acknowledgements

Abstract

Second Harmonic Generation (SHG) microscopy is a powerful non-linear optical microscopy technique that has made significant strides in the field of biological imaging. The principle of SHG microscopy is based on the process of second harmonic generation, where two photons combine in a non-centrosymmetric medium and emit a photon with twice the energy, hence, half the wavelength, contributing to the generation of higher resolution images. SHG microscopy can also be used to image the characteristics of ferroelectric domains, making it vital for modern nonlinear and quantum optical studies in ferroelectric materials such as lithium niobate.

Poling is a technique utilized to alter the characteristics of ferroelectric materials, such as lithium niobate: this method involves the application of a strong electric field to the material, thereby initiating an alignment process of the material's spontaneous polarization within its domains. Periodically poling the material with alternating domains is vital in facilitating efficient nonlinear optical processes, from second harmonic generation to optical parametric amplification. This configuration is designed to facilitate quasi-phase-matching (QPM) within the material, a key element in boosting SHG efficiency. Notably, this technique's success is contingent on various parameters of the biasing pulses, such as their amplitude, duration, rise and fall times. To investigate more deeply which of these factors more heavily influence the quality of poling, it is extremely useful to be able to image the ferroelectric domains' depth through SHG microscopy; the purpose of this Master Thesis was to design such a tool.

To enable the design of a SHG microscope, a comprehensive understanding of the fundamental physical principles underlying second harmonic generation was first achieved. This involved delving into the non-linear optical processes that give rise to this phenomenon, enabling a good understanding of the mechanisms contributing to the generation of the second harmonic signal. Subsequently, an extensive review of the current literature and technical datasheets was undertaken. This allowed for an in-depth understanding of the state-of-the-art SHG microscopes currently available, including the design principles, the components used, and the operational techniques employed. This literature review helped identify key components and standard practices, as well as recognize potential areas for improvement or modification.

The subsequent implementation of the instrument produced satisfactory results: the sample can effectively be scanned with our laser, imaged through wide-field channels with adequate magnification, and can produce an observable SHG signal.

In conclusion, this SHG microscope promises to drive significant advancements in the study of periodic poling in lithium niobate and related materials. By facilitating high-resolution, non-destructive imaging of these domains, this work will enable a deeper understanding of the material's behavior post-poling.

Glossary

galvo A galvanometric scanner, or galvo, is an electromechanical device used to rapidly and precisely control the direction of laser beams or light sources in various applications. 2

Acronyms

APD Avalanche PhotoDiode. 2

emu ElectroMagnetic Units. 2

FOV Field Of View. 2

HWP Half Wave Plate. 2

LN Lithium Niobate. 2

PMT PhotoMultiplier Tube. 2

PPLN Periodically Poled Lithium Niobate. 2

PSF Point Spread Function. 2

SHG Second Harmonic Generation. 2

Contents

Chapter 1

Introduction

The introduction will begin from an overview of integrated photonics, that is the application justifying all the effort spent on building a SHG microscope. Once the general context is clear, it will delve more into the theoretical physical foundations of this work; the final part aims at providing a more precise explanation of some specific practical aspects and the workflow.

1.1 General overview on integrated photonics

Integrated photonics, also known as integrated optics, is a technology that combines or integrates multiple photonic functions, such as light generation, modulation, amplification, and detection, on a single chip. This technology is analogous to electronic integration, which has revolutionized the electronics industry by enabling the development of complex electronic circuits and systems on a single silicon chip.

The field of integrated photonics has seen significant advancements over the past few decades, driven by the increasing demand for faster, more efficient, and smaller devices in various applications, including telecommunications, data communications, sensing, and computing. Integrated photonic devices offer several advantages over their discrete counterparts, including smaller size, lower power consumption, higher reliability, and potentially lower cost due to mass production.

One of the key materials used in integrated photonics is lithium niobate ($LiNbO_3$). Lithium niobate is a unique material that exhibits excellent electro-optic, **nonlinear**, and piezoelectric properties, making it an ideal material for a wide range of photonic devices. For instance, its strong electro-optic effect is utilized in modulators for high-speed optical communications, while its high nonlinear optical coefficients are exploited in frequency converters for laser systems.

In recent years, lithium niobate has gained renewed interest due to the development of lithium niobate on insulator (LNOI) technology, which allows the fabrication of high-performance photonic integrated circuits on thin lithium niobate films. This technology combines the superior photonic properties of lithium niobate with the advantages of the planar technology used in silicon photonics, such as high integration density and compatibility with CMOS fabrication processes.

Moreover, lithium niobate waveguides, which are key components of lithium niobate integrated photonic circuits, have been extensively studied for various applications. For example, they have been used to create efficient second harmonic generation (SHG) devices [9], which are important for frequency conversion.

1.2 Nonlinear Optics

To gradually introduce the topic of this thesis, it is important to start from the basic physics behind the project; as already stated, nonlinearity is one of the most interesting properties of LiNbO$_3$ and it lies at the core of SHG microscopy, therefore it will be introduced in the following paragraph, and treated like in [1]. Nonlinear optics studies the alteration of a material's optical properties due to light, typically intense laser light. This field began with the discovery of second-harmonic generation after the first working laser demonstration. Nonlinear optical phenomena occur when a material's response to an optical field is nonlinearly dependent on the field's strength. For example, in the process of second-harmonic generation, the behavior of atoms is determined by the square of the optical field strength applied; as a result, the intensity of light at the second-harmonic frequency grows with the laser light intensity squared. On the other hand, in linear optics, the generated polarization is directly in line with the strength of the electric field, as expressed in Equation 1.1.

$$\tilde{P}(t) = \chi^{(1)} \tilde{E}(t) \tag{1.1}$$

where the constant of proportionality $\chi^{(1)}$ is known as the linear susceptibility[1]. In nonlinear optics, a more general relation can be written, describing χ as a power series[2]:

$$\begin{aligned} \tilde{P}(t) &= \chi^{(1)} \tilde{E}(t) + \chi^{(2)} \tilde{E}^2(t) + \chi^{(3)} \tilde{E}^3(t) + \cdots \\ &\equiv \tilde{P}^{(1)}(t) + \tilde{P}^{(2)}(t) + \tilde{P}^{(3)}(t) + \cdots \end{aligned} \tag{1.2}$$

$\chi^{(2)}$ and $\chi^{(3)}$ are known as the second and third order nonlinear susceptibilities; equivalently $\tilde{P}^{(2)}(t)$ and $\tilde{P}^{(3)}(t)$ are known as second-order and third-order nonlinear polarization. $\tilde{P}^{(2)}(t)$ appears only in noncentrosymmetric crystals, i.e. those that do not display inversion symmetry, therefore liquids, gases and amorphous solids will not produce SHG light. Let's now do an order of magnitude evaluation of $\chi^{(2)}$; $\chi^{(1)}$ is usually close to unity; a reasonable assumption, for an electric field in the order of E_{at}, is to assume $\tilde{P}^{(2)}(t)$ to be close to $\tilde{P}^{(1)}(t)$. This implies that $\chi^{(2)}$ must be of the order of $\chi^{(1)}/E_{at} \sim 1/E_{at}$, where E_{at} is the characteristic atomic electric field strength, calculated as $E_{at} = e/a_0^2$, with

---

[1] Equation 1.1 is valid for a material with an instantaneous response. A more complex formulation involving a convolution with the response function must be included in the general case.

[2] Here we are considering a 1-dimensional field, therefore the susceptibilities are constants, but this can be extended to the 3-dimensional case, where $\chi^{(n)}$ would be tensors. Another assumption is made, that the medium is lossless and dispersionless, therefore it responds instantaneously to the input field and thus the polarization $\tilde{P}(t)$ depends only on the instantaneous value of the electric field $\tilde{E}(t)$.

a_0 being the Bohr radius of the Hydrogen atom and e is the magnitude of the electron charge. This turns out to be quite realistic ($\chi^{(2)} \sim 5 \times 10^{-8}$ emu and $\chi^{(3)} \sim 3 \times 10^{-15}$ emu). The most common approach to describe nonlinear optical interactions is by means of polarization. As denoted in Eq. 1.3, which relates $\tilde{P}^{(NL)}(t)$ to the electric field, the nonlinear polarization acts as a source of nonlinear electric field in the sense that if $\frac{\partial^2 \tilde{P}^{\text{NL}}}{\partial t^2}$ is different from 0, charges are accelerated, thus producing an electromagnetic wave.

$$\nabla^2 \tilde{E} - \frac{n^2}{c^2}\frac{\partial^2 \tilde{E}}{\partial t^2} = \frac{4\pi}{c^2}\frac{\partial^2 \tilde{P}^{\text{NL}}}{\partial t^2} \tag{1.3}$$

1.2.1 SHG

Second-harmonic generation is a nonlinear optical process involving the conversion of a laser beam's electric field strength into a second harmonic, as depicted in Figure 1.1.
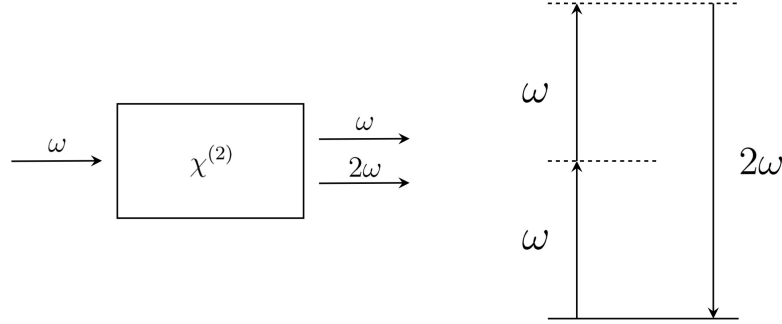
Figure 1.1: SHG block diagram (left) and energy diagram (right).

The field incident on the nonlinear crystal can be written as:

$$\tilde{E}(t) = E e^{-i\omega t} + E^* e^{i\omega t} \tag{1.4}$$

The second-order nonlinear polarization $\tilde{P}^{(2)}(t)$ will be given by Eq. 1.2, leading to:

$$\tilde{P}^{(2)}(t) = 2\chi^{(2)}EE^* + \left(\chi^{(2)}E^2 e^{-2\omega t} + \chi^{(2)}E^{*2}e^{2\omega t}\right) \tag{1.5}$$

The first term is a constant, therefore its second time derivative will be null, and it will not contribute to SHG (according to Eq. 1.3); it will only produce a phenomenon known as optical rectification, which creates a static electric field in the nonlinear material. The second term is varying with time instead, and it has a non null time second derivative, thus producing second harmonic light at a frequency 2ω.

The concept of second-harmonic generation involves the exchange of photons between different frequency components of the field. In this process, two photons of frequency "ω" are eliminated, while a photon of frequency "2ω" is simultaneously created. This

quantum-mechanical phenomenon can be visualized using a diagram (in Fig. 1.1), where the solid line represents the atomic ground state, and the dashed lines depict virtual levels that represent the combined energy of the atom's energy eigenstates and photons from the radiation field. SHG efficiency is generally low; the generation of the second harmonic is a nonlinear process, meaning that it only occurs effectively under specific circumstances, such as high intensity light or very long interaction distances. In nonlinear optical processes like SHG, the efficiency is strongly dependent on the phase velocity matching between the interacting waves at different wavelengths. However, due to dispersion in most materials, these interacting waves can quickly get out of phase, reducing the efficiency. Considering again the interactions between photons pictured in Fig. 1.1, the energy is always conserved, but the probability of the process depends on the conservation of momentum, so the larger the momentum mismatch ($\Delta k = k_{2\omega} - 2k_{\omega} = \frac{4\pi}{\lambda}(n(2\omega) - n(\omega))$), the smaller the efficiency will be. The traditional solution is to use birefringence in a crystal to compensate for this dispersion, but this approach has some limitations, such as a restricted choice of wavelengths and polarization.

Quasi-Phase Matching (QPM) offers an alternative solution. In QPM, the sign of the nonlinearity is periodically reversed and the additional momentum is provided by the wave vector of the periodic structure. This means having a spatial variation of the effective nonlinear coefficient of the following type:

$$d(z) = d_{\text{eff}} \, \text{sign}[\cos(2\pi z/\Lambda)]. \tag{1.6}$$

It can also be expressed as a Fourier series:

$$d(z) = d_{\text{eff}} \sum_{m=-\infty}^{m=\infty} G_m \exp(ik_m z) \tag{1.7}$$

where Λ is the period of the structure, while $k_m = 2\pi m/\Lambda$ is the m-th order grating vector. The primary Fourier vector is equal to $2\pi/\Lambda$ and is responsible for the momentum compensation; therefore, it has to be set equal to $\Delta k = k_{2\omega} - k_{\omega}$; the reversal is typically achieved through a process known as periodic poling. Periodic poling involves changing the polarity (the polarization vector direction) of a nonlinear crystal at regular intervals along the direction of light propagation. This is typically done by applying a high electric field to the crystal. The result is a nonlinear crystal that can support efficient nonlinear optical processes at a much wider range of wavelengths than is possible with traditional phase matching.

1.3   PPLN (Periodically Poled Lithium Niobate)

Periodically Poled Lithium Niobate (PPLN) is a highly efficient medium utilized for nonlinear wavelength conversion processes. These processes include frequency doubling, difference frequency generation, sum frequency generation, among others. The crucial aspect of these processes is phase matching, achieved through Periodic Poling. It ensures the relative phase between two or more frequencies of light remains constant as the light propagates through the crystal; PPLN finds its application in devices such as Optical

Parametric Oscillators (OPOs), which use a pump laser at λ to produce signal and idler beams at any wavelength longer than the pump laser wavelength. PPLN is also used for Second Harmonic Generation, where it has demonstrated the ability to frequency double pulsed beams with high conversion efficiency.
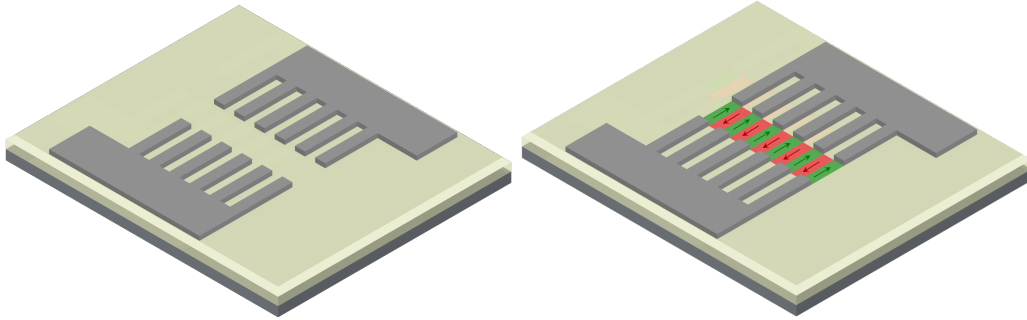
Figure 1.2: Schematic view of poling electrodes deposited on top of LN. Unpoled structure (left) and poled structure (right). The LN layer was labeled with red and green colors to differentiate the periodically inverted ferroelectric domains, or left unaltered (yellow) for non-polarized parts.
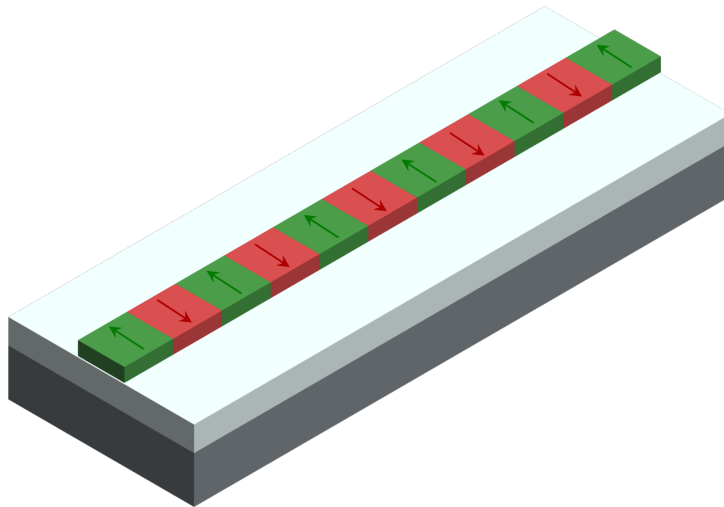
Figure 1.3: Illustration of a PPLN waveguide.

1.4   Purpose of the project

The examination of poling quality, specifically the depth[3], in lithium niobate waveguides is of paramount importance, as it is of fundamental importance for the development of

---

[3]The term "poling depth" refers to the maximum depth at which polarization occurs due to the voltage applied via surface electrodes on the Lithium Niobate (LN) layer. Beyond this depth, the electric field

devices.

The study by M. Rusing [10] underscores the necessity of comprehending the complexities of periodically poled thin films. The authors suggest that second-harmonic (SH) microscopy is indispensable for gaining insights into these structures. This understanding is pivotal as it facilitates the engineering and design of PPLN structures, which are integral to nonlinear optical frequency conversion processes via the quasiphase matching (QPM) technique.

The authors then explain that the success of QPM depends on the fabrication of high-quality ferroelectric domain grids over a millimeter to centimeter scale. This necessitates a thorough understanding of the domain fabrication process, which is aided by visualization and analysis tools such as SH microscopy. Therefore, the assessment of poling quality is vital for ensuring the efficacy of these processes.

The paper presents an in-depth analysis of SH microscopy in x-cut lithium niobate thin films, incorporating a full three-dimensional focus calculation accounting for interface reflections, to calculate the nonlinear polarization and then the SH light. The authors demonstrate that the dominant signal in back-reflection originates from a copropagating phase-matched process observed through reflections, as opposed to direct detection of the counterpropagating signal as seen in bulk samples; the result of these processes leads to an interference pattern in the regions where poling does not reach the bottom of the LN layer. This finding underscores the importance of assessing the poling quality to ensure the efficacy of the SHG process.

Therefore, the aim of this project was to design a SHG microscope specific for $LiNbO_3$, which will allow to investigate the quality of poling while actually performing it.

1.5 Workflow

In order to tackle a complex task such as building a measurement instrument, the workflow was spontaneously divided into different consecutive phases. The **first phase** was a literature review (first part of Chapter 2) to better frame the problem, understanding all the aspects involved in the project. It served as a vital component in establishing the foundation of my work because it allowed to get a better understanding of the topic, explore similar solutions that have already been adopted to understand the main parameters of the project space, and find original solutions that had not been investigated yet.

The **second phase** (second part of Chapter 2) consisted of designing a high-level scheme of the final instrument. This was essential to fix the scheme and start working on the search for components that could do the high-level job they were attributed in the scheme and fit into the overall design. This involved researching and evaluating various options available in the market, considering factors such as cost, performance,

---

has no impact on the material. An intuitive understanding of this concept can be obtained from Figure 1.2.

availability[4], and compatibility with the rest of the instrument. Furthermore, this phase allowed for the identification of any potential challenges or limitations that may arise during the implementation of the instrument. Addressing these issues early on allowed developing strategies or alternative solutions to overcome them in later stages. After this phase, all the needed components of the block diagram were purchased.

The **third and final phase** (Chapter 3), was devoted to building the instrument itself, coordinating every component to each other, doing experiments and measurements to test every part and make sure it worked as designed.

---

[4]Many components had very long lead times, which are incompatible with the limited time available for this project.

Chapter 2

Literature review & Design

In order to fully understand the physics behind the instrument and determine the key parameters for SHG imaging, an initial deep and thorough literature review of the state-of-the-art instruments has been carried out. After a first phase devoted to sharpening the knowledge about optical scanning imaging systems, the search was narrowed to multiphoton microscopy and finally to SHG microscopy. That allowed the generation of a high-level schematic representation of the instrument (Fig. 2.1) and the most important variables and components needed (Tab. 2.2), which will be discussed in this chapter.
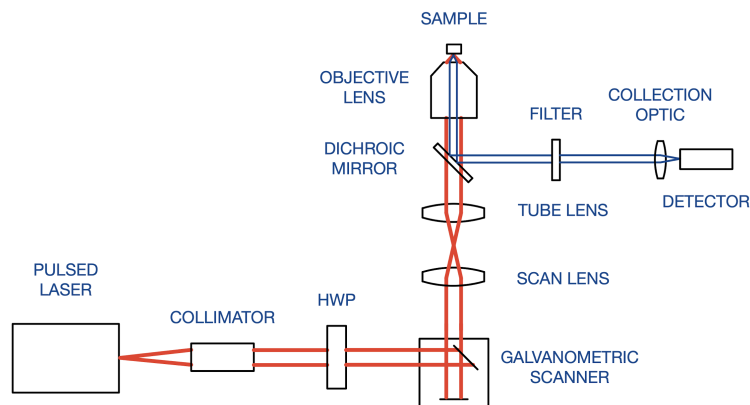

Figure 2.1: Block diagram of the instrument

2.1 Design space

The very first phase of the research consisted of finding the factors that seemed most relevant to the project. They constituted the design space and sometimes interfered with each other and could not be chosen independently. They will be treated in the following sections and for each of them the main parameters will be highlighted, explaining how

Component	Parameters
Laser source	Wavelength
	Power
	Pulse width
	Polarization
Objective lens	Numerical aperture
	Working distance
Filter	Center wavelength
	Rejection performance
Dichroic Mirror	Cut-on wavelength
Scanning mechanism	Scanning speed
	FOV
Detector	Wavelength range
	Sensitivity
	Noise

Table 2.1: Component Parameters (The detector is discussed in Sec. 2.2).

they affect the instrument.

2.1.1 Different schemes of already existing experimental apparatuses

Some of the already existing experimental setups for SHG imaging are shown in Fig. 2.2.

The first one (top-left) comes from [7], and it is a transmission microscopy setup; two different objectives are therefore used (the first one has a lower NA and is only used to focus light on the sample, the second one has a higher NA and collects the transmitted light). A HWP is used to rotate the polarization along the crystallographic axis where the nonlinear coefficient is the highest. The SHG is separated from the FH through a dichroic mirror and then filtered again before being acquired by a PMT tube. The top-right [5] setup includes the scanning system mirrors, which reflect light coming from their pulsed Ti:Sapphire laser onto the objective back aperture, the SH light is then collected and filtered through a condenser lens and a filter and measured by means of a PMT tube coordinated by a computer. In the bottom left setup [3] the principle is the same of the first 2 setups but a confocal pinhole is added to only capture light coming from the focal plane, rejecting out-of-focus light from the sample. The bottom right image [10] is also very similar to the already discussed setups, but a better view of the sample is provided. The SHG light measured by the detector in reflection configuration will be a result of many physical processes of interference and resonance, already mentioned in Sec. 1.4.
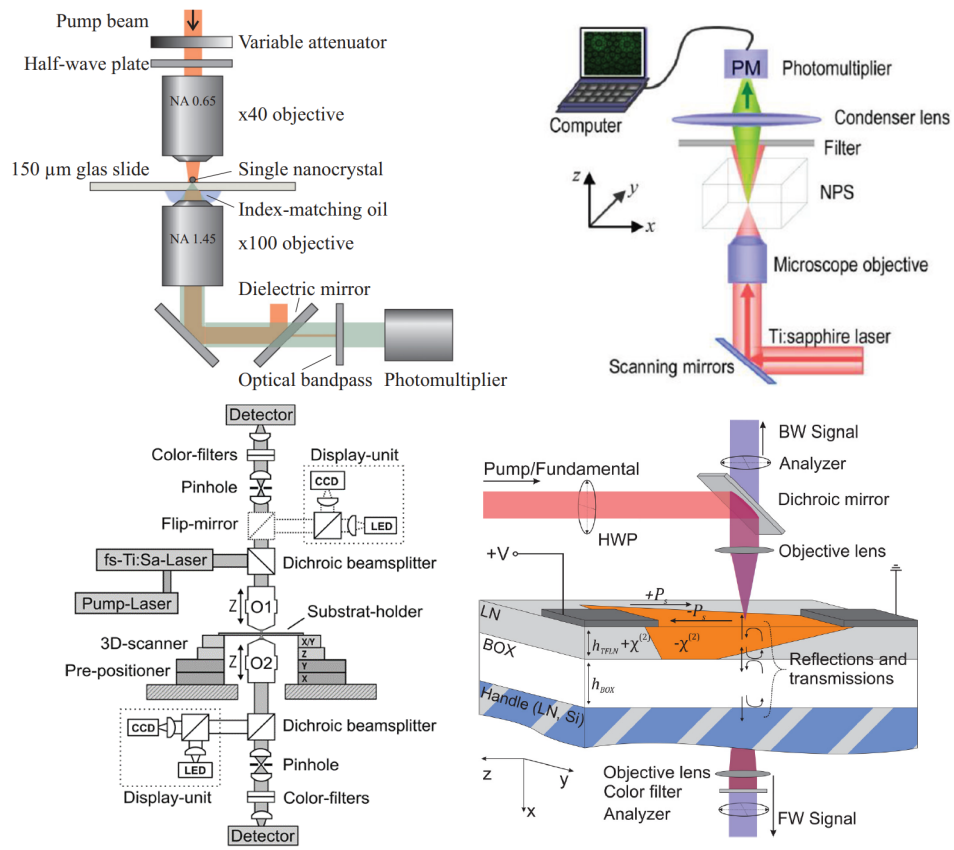
Figure 2.2: Different experimental setups implementing SH imaging.
Top left: [7], Top-right: [5], Bottom-left: [3], Bottom-right: [10].

2.1.2 Wavelength

The wavelength required for performing second harmonic (SH) imaging of periodically poled lithium niobate (PPLN) does not appear to be a significant parameter as long as the fundamental beam is tightly focused, as mentioned in [5]:

> "It is known that in the regime of a tightly focused fundamental beam, the Cerenkov process is insensitive to the wavelength of the fundamental wave. Therefore, this imaging system can operate at a wide range of wavelength limited only by the absorption edge of second harmonic and the total reflection condition."

To investigate the observability of SHG at longer wavelengths, a different article [8] demonstrates the utilization of 1617 nm light to induce SHG.

While most literature sources primarily employ 800 nm light as the primary radiation source when studying SH generation in lithium niobate (e.g. in [3]), potentially due to its better lateral resolution, a study presented in [7] employs 1064 nm light (as shown in the figure below) to illuminate LN crystals and collect the SH signal for $\chi^{(2)}$ characterization. Additionally, in [14], an Ando AQ4320D Tunable Laser with a wavelength range of 1520-1620 nm is employed, although imaging is not the focus of this investigation.
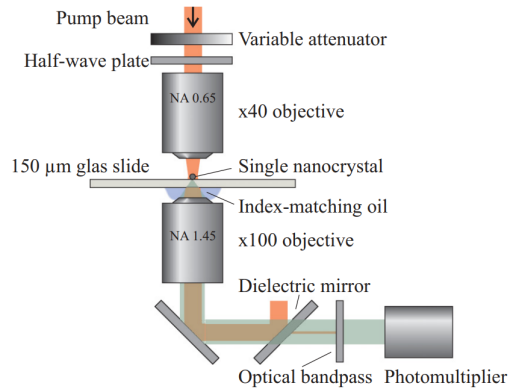

Figure 2.3: Experimental imaging apparatus in [7], using 1064 nm wavelength to retrieve information about $\chi^{(2)}$ in LN crystals

Therefore literature indicates that there are no valid reasons to avoid using larger wavelengths, except for a decrease in lateral resolution (based on the Rayleigh formula) and depth resolution.

2.1.3 Pulse parameters

Power

Power has a very important role in the SHG process: in [6], it is found that, considering a plane wave approximation for the incident field, the dependence of the second harmonic power $P_{2\omega}$ is given by the following equation:

$$P_{2\omega} = \chi_2 \cdot \frac{P_\omega^2}{A} \cdot \frac{32\pi^3\omega^3}{c^3\epsilon(\omega)\sqrt{\epsilon(2\omega)}} \left(\frac{sin\left(\Delta kL/2\right)}{\Delta kL/2} \right)^2 \tag{2.1}$$

This analysis shows that the second harmonic optical power is proportional to the square of the instantaneous peak power at the input, which is why femtosecond lasers are utilized. In the case of the same average power, a shorter pulse generates a higher emission. Furthermore, it is mentioned in the article that "*For SHGI, pulses as short as possible are desirable.*" As a point of reference, in the aforementioned article, a power of 50 mW at 800 nm (Ti:Sapphire laser) is employed.

Pulse Energy

Pulse total energy does not seem to be relevant per se, as the pulse instantaneous peak power is the crucial parameter for SHG, i.e. the pulse duration.

Pulse width

No lower limit for the pulse width was identified in the study: it was noted that the second harmonic generation (SHG) light is generated within a few femtoseconds (fs). As previously mentioned, there is a preference for shorter pulse durations in the context of SHG imaging (SHGI). Reference values for pulse widths typically range between 100-150 fs.

In conclusion, it can be observed that increasing the power within acceptable limits (without causing damage to the sample) results in amplified second harmonic generation (SHG) signals and subsequently improved signal-to-noise ratio (SNR).

2.1.4 Polarization

The polarization of the fundamental harmonic (FH) light is crucial for maximizing the generation of the second harmonic (SH) signal. The most common choice [3] is using a **linear polarization**, directed along the crystallographic axis of Lithium Niobate where the nonlinear coefficient is the highest (d_{33}, along the crystallographic z-axis).

2.1.5 Objective lens

Objective lenses play a crucial role in scanning microscopy. These lenses are specially designed to focus light onto the sample and collect light generated from it, ensuring high-resolution imaging. The use of objective lenses in confocal microscopy enables the formation of a focused spot of light that can be scanned across the specimen in a controlled manner; in the specific case of SHG microscopy, the part of the sample that is illuminated by the light coming from the objective will be the only area where the light power is large enough to generate a detectable SH signal, that will be collected from the same objective and measured by a single element detector. The narrowness of the region illuminated

17

by the objective lens is quantified by a number, called **numerical aperture** (NA). The effect of a high-NA objective will be to:

- Increase lateral resolution ($|x_{min}| = \frac{0.46\lambda}{NA}$[1]).

- Increase the peak signal intensity – the spot size should be reduced as much as possible so that the power is concentrated in a smaller area and therefore the peak value is higher (and so greater SHG signal).

2.1.6   Dichroic Mirror & Filter

A dichroic mirror and a bandpass filter are essential components in any multiphoton microscope[2]. The first comes from the need for an optic capable of transmitting the pump light (at longer λ), and reflecting the nonlinearly generated light at higher energy (at lower λ) with great efficiencies. More specifically, longpass[3] dichroic mirrors are used. Filters are used to further sharpen the division between SH and FH light, and can also eliminate stray components of light coming from the environment or unwanted reflections.

Selection of independent elements

At this stage, the block diagram in Fig. 2.1 was made and a significant portion of the components was selected. The laser, which is typically the most expensive part of the setup, has been chosen as the starting point, meaning that the available laser (FSL1010) was utilized for the experiment. It is a 1550 nm pulsed laser capable of delivering 150 fs pulses with a repetition rate of 80 MHz, and an average power of 10 mW. Since FSL1010 is a fiber-coupled laser, a collimator is needed to couple light into free space. For this purpose F240APC-1550 was used. It allows to collimate the light coming from the fiber with a reasonable divergence (see Fig. 2.6).

As already discussed at the beginning of Sec. 2.1.1, a HWP is important to rotate the light polarization and align it along the z-axis of LN, to obtain a larger signal. A product implementing this function is WPH05M-1550, that was combined to PRM1 to precisely tilt the polarization. Another component that is readily selectable at this point is the dichroic mirror. Its purpose (shown in Fig. 2.1) is to transmit the FH pump light (1550 nm) and reflect the SH light (775 nm) generated by the sample in order to redirect it onto the detector; therefore, a longpass dichroic mirror is needed, that is to say a mirror able to reflect lower wavelengths and transmit longer ones. The cut-on wavelength is not crucial and has been chosen somewhere between the FH and SH, at 950 nm. In Fig. 2.4 the reflection and transmission spectra of the chosen component have been plotted.

---

[1]This formula is analyzed in 2.1.7.

[2]A multiphoton microscope is one of the ways instruments involving the interaciton of 2 or more photons are called. It operates with pulsed lasers on the principle of multiphoton excitation, where two or more photons interact simultaneously with a fluorophore, resulting in the emission of a higher-energy photon.

[3]Longpass indicates that the optic has a cut-on wavelength, above which photons are transmitted, and below which are reflected.
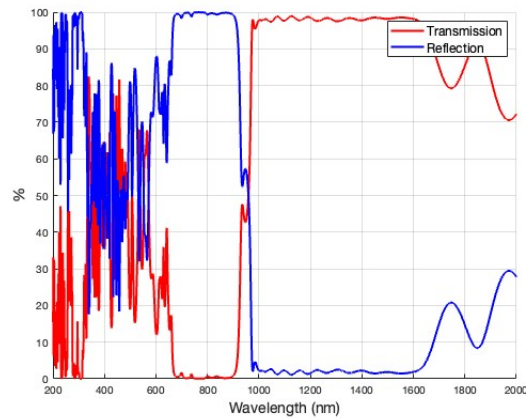
Figure 2.4: T and R spectra of the dichroic mirror; raw data was provided by Edmund Optics upon request.

A further filtering stage is generally used to suppress the FH signal at the detector; in our case a FESH0900 has been used. It is a shortpass filter with a 900 nm cutoff wavelength (spectrum in Fig. 2.5). After the light is properly filtered, it must be focused on the photosensitive part of the detector, since its surface is generally very small. For this purpose a simple lens can be used, just like LBF254-075. A summary of this part of the design is found in Tab. 2.2.
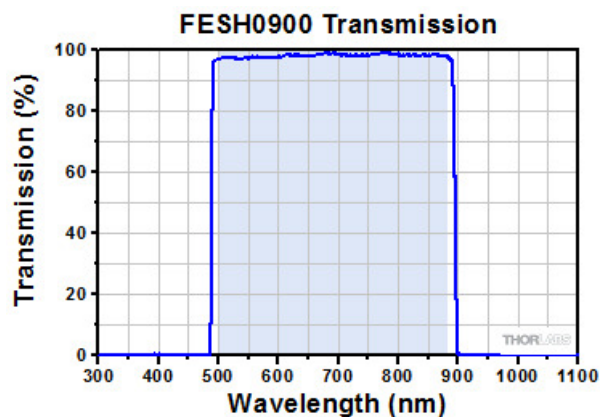
Figure 2.5: FESH0900 transmission spectrum.
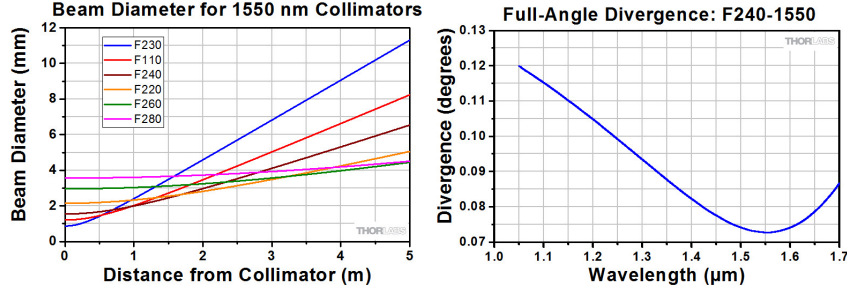
Figure 2.6: Beam diameter as a function of the beam path length, for different collimators (left), divergence of the selected collimator as a function of the wavelength (right).

2.1.7 Design of scanning system and Objective selection

In the previous section some of the already existing experimental apparatuses for multi-photon microscopy were shown. Some key elements are common to all these setups:

- Pulsed laser as pump

- Scanning system (not depicted in all the figures)

- Objective lens

As opposed to the laser source and the other components discussed in the previous section, the objective and scanning system need more calculations to be selected and used in combination to each other. In order to get an overall working system the objective choice had to be performed together with the scanning system design because, as it will be described in the following section, the scan and tube lenses' focal lengths will influence the beam diameter, which needs to be chosen accordingly to the objective lens, in order to fill out its back aperture.

The design can start from a first choice of the objective lens depending on the needed numerical aperture, which will determine the resolution of the microscope. Starting from the resolution, the minimum difference of two different features that can be successfully resolved through light at a wavelength λ with an objective lens of numerical aperture NA is given by the Rayleigh criterion:

$$d = \frac{0.61\lambda}{\text{NA}} \tag{2.2}$$

This formula comes from the assumption that two objects can be considered resolved if the peak of one object's diffraction pattern falls on the first minimum of the diffraction pattern of the other object; the PSF generating the diffraction pattern in nonlinear phenomena has to be elevated to the N-th power, with N being the order of the nonlinear phenomenon under consideration ($N = 2$ for SHG).

The formula for resolution thus can be rewritten as:

$$d^{(N)} = \frac{1}{\sqrt{N}} \frac{0.61\lambda}{\text{NA}} \tag{2.3}$$

A more precise formula (Eq. 2.4) is necessary for high NA ($NA > 0.7$), for which the paraxial approximation starts to give not as precise results anymore [13].

$$w_{xy} = \begin{cases} \dfrac{0.32\lambda}{\sqrt{2}NA} & \text{if } NA \leq 0.7 \\ \dfrac{0.325\lambda}{\sqrt{2}NA^{0.91}} & \text{if } NA > 0.7 \end{cases} \tag{2.4}$$

Once the resolution is chosen, the NA can be selected, or conversely, the NA can be chosen and the acceptability of the resolution can be assessed afterwards. An objective is then selected based on this resolution, and the remaining parameters of the scanning system can be tuned accordingly.

From [13] we have that the following inequalities (Eq. 2.13) must be satisfied, for f_t (the tube lens focal length) and A_t (the tube lens aperture). A small derivation is provided in the following for a better understanding of what these constraints imply (expanding and explaining what is treated in [13]). The general picture is that of a 4f-like system (2.7), constituted of a scan lens (on the left) and a tube lens (on the right). The distance between the galvo mirrors and the scan lens will be equal to the scan lens focal length, while the distance between the objective aperture and the tube lens will be equal to the tube lens focal length; the two lenses are separated by a distance equal to the sum of the two focal lengths. In such a way, if the laser beam is correctly collimated at the input of the system, it will still be at the output.
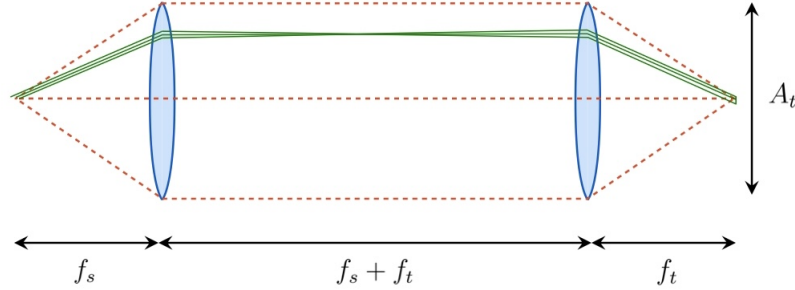

Figure 2.7: 4f system.

The first notion that should be remembered is the one depicted in 2.8:

$$\Delta = f \tan \theta \approx f\theta, \text{ if } \theta \text{ is very small} \tag{2.5}$$

To derive Eq. 2.13, it is sufficient to observe Fig. 2.9: the maximum angle deflection provided by the galvo mirror θ_{MAX} will imply the maximum displacement Δ, which will in turn define the largest angle of the beam exiting the tube lens. That maximum angle influences the FOV on the sample (because according to Eq. 2.5 the largest incidence angle of light on the objective lens will result in the largest displacement of the focused

21
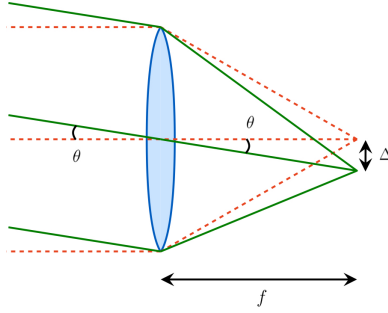
Figure 2.8: $\sin\theta \sim \theta$ approximation

laser spot on the sample). It is then possible to write a relation between these maximum quantities[4]:

$$\frac{A_t}{2} \geq \underbrace{f_t\theta_{MAX}}_{\Delta} + \underbrace{\frac{D_b}{2}}_{\text{Beam size}} \tag{2.6}$$

From here:

$$A_t \geq 2f_t\theta_{MAX} + D_b \tag{2.7}$$

Regarding the objective, we can write:

$$\frac{A_o}{2} = f_o\sin\theta = f_oNA \rightarrow A_o = 2f_oNA \rightarrow A_o = 2f_oNA \tag{2.8}$$

The maximum displacement Δ on the sample surface (consider Fig. 2.8 with the objective lens) will be given by:

$$\Delta = f_o\tan\theta_{MAX} \approx f_o\theta_{MAX} \tag{2.9}$$

We define now the *FOV* as $FOV = 2\Delta_{MAX} = 2f_0\theta_{MAX}$, that is to say the portion of the sample that can be reached by the focused laser.

Assuming that the beam diameter is as big as the objective back aperture (since it has to be filled out in order to exploit its full numerical aperture), we can rewrite Eq. 2.6 as:

---

[4]All the following equations are retrieved for the case of tube and scan lenses with the same focal length, but the explanation can be easily generalized to the case of different focal lengths by just introducing a magnification factor given by the ration of the focal lengths. Its effect will be of giving a deflection angle after the tube lens given by the incidence angle of light on the scan lens, multiplied by that multiplication factor. Equivalently the beam diameter of the beam exiting the tube les will be given by the beam diameter before the scan lens divided by the magnification factor.

$$A_t \geq 2f_t\theta_{MAX} + D_b = 2f_t \cdot \frac{FOV}{2f_o} + A_o = \frac{f_t}{f_o}FOV + 2f_oNA \tag{2.10}$$

It is generally convenient to express the objective focal length as $f_o = f_t'/M$, where f_t' is the focal length of the manufacturer-prescribed tube lens, and M is the magnitude provided by the combination of the objective with that lens.

Equations 2.10 and $f_o = f_t'/M$ allow us to calculate the necessary aperture of the tube lens, given the desired field of view (FOV) and the measurable parameters from the objective lens, namely the magnification and the numerical aperture (NA), by means of Eq. 2.11.

$$A_t \geq \frac{f_t}{f_t'}MFOV + 2NA\frac{f_t}{M} \tag{2.11}$$

While Equation 2.11 provides a convenient guideline for selecting the aperture of the tube lens, the aperture is typically predetermined (because it depends on the size constraints given by the instrument one is building), and the focal length of the tube lens becomes the variable parameter. Hence, it is more convenient to reorganize this expression as follows:

$$f_t \leq \frac{f_t'}{M^2\mathrm{FOV}}\left(A_tM - 2\mathrm{NA}f_t'\right) \tag{2.12}$$
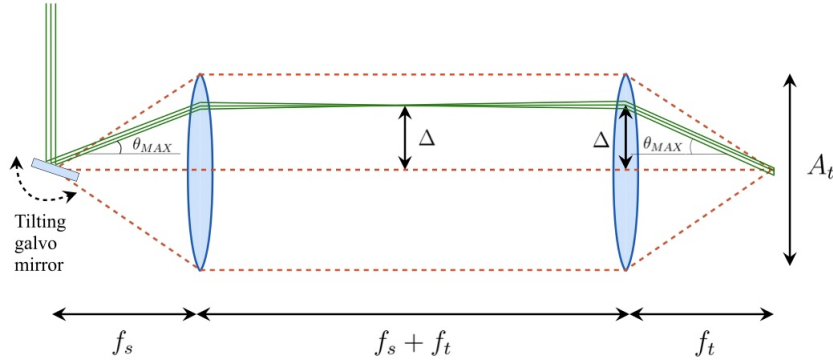
Figure 2.9: 4f-like system constituted by the scan lens and the tube lens. The represented case is that of a matched scan and tube lens (with the same focal length).

$$\begin{cases} A_t \geq \dfrac{f_t}{f_t'}M \cdot FOV + 2NA\dfrac{f_t'}{M} \\[2mm] f_t \leq \dfrac{f_t'}{M^2FOV}\left(A_tM - 2NAf_t'\right) \end{cases} \tag{2.13}$$

On THORlabs' website, there is a dedicated section for tube lenses designed to be used in conjunction with infinity-corrected objectives for scanning purposes. The prescribed focal length, denoted as f_t', is 200 mm and since we do not have any particular requirement

for the objective magnification[5], we can use the tube lens suggested by the manufacturer, so we have $f_t \equiv f_t'$.

The value of A_t is typically predetermined by the type of setup being constructed, such as the cage being used.

Once A_t is determined, we can calculate the maximum f_t based on the magnification provided by the microscope, the numerical aperture (NA), and the desired field of view (FOV). According to our needs, the FOV should range from 100-200 μm to 700 μm. The FOV is determined by the maximum Δ achievable on the sample, which depends on the maximum angle θ_{max} that the galvo system can achieve. The relationship is described by the equation below:

$$FOV = 2\Delta_{max} = f_o\theta_{max} \tag{2.14}$$

From here one can also decide the scan lens (and if needed provide a magnification or demagnification by choosing the ratio between the scan lens and tube lens focal lengths. Either choosing one of the two solutions, or not introducing a mismatch at all will be dictated by the galvo system. If the error in the angle is very small one can perform a magnification, if it is significant, do a demagnification; otherwise, just use matched lenses.)

After searching different optics sellers, the choice was to use:

- TL200-3P

  - f: 200 mm
  - A_t: 47 mm
  - λ range: $[900 - 1900 \; nm]$

- SL50-3P

  - f: 50 mm
  - A_t: 27 mm
  - λ range: $[800 - 1800 \; nm]$

- A galvanometric scanner commonly used for laser projection[6]

  - Max scan speed: 30 kpps

---

[5]In this case, the magnification M introduced by the objective (that should not be confused with the magnification factor of the 4f system) is not important because, as previously stated, the size of the laser spot on the sample is "mapped" to the size of the laser emitted by the objective. Since we are not acquiring the full image of the sample at once (illuminating the entire sample) but rather scanning each point of the surface, all the light generated for each scan point is attributed to the specific voxel being considered. It could be necessary to ensure that the size of the light beam does not exceed the detector size, as some signal would be lost in that scenario.

[6]Some measures were taken in order to make it work for our application, they are described in Sec. 3.4.2.

– Max angle of deflection: $18°$[7]

- [MY50X-825](#)

  – Back aperture: 3.36 mm[8]

  – Magnification: 50

  – λ range: $[480 - 1800\ nm]$[9]

  – Working distance: 17.0 mm[10]

If we substitute the values of the selected components into Eq. 2.13 (and choosing a FOV of 350 μm) we obtain $f_t \leq 501.03$ mm; $f_t = 200$ mm for TL200-3P, therefore the constraint is satisfied. The beam diameter after the 4f-like system is acceptable too.
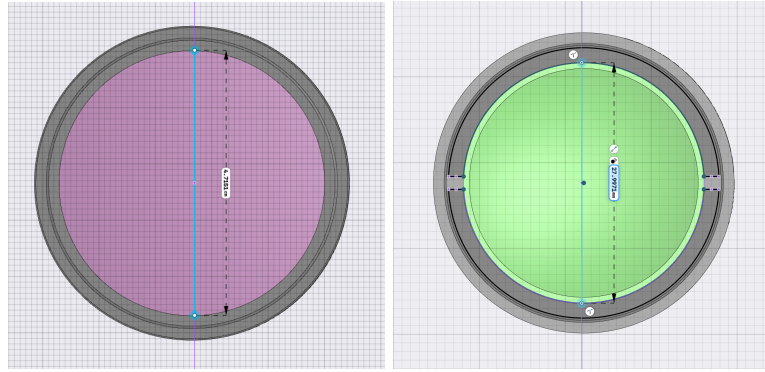

Figure 2.10: Tube lens and scan lens aperture measured from the CAD file.

The scanning system constituted by the chosen elements is telecentric, which is extremely important in the design of this instrument. In the case of scanning microscopy, telecentricity is needed in order to ensure that the laser spot is circular even when the laser beam comes onto the objective back aperture with an angle (Fig. 2.11); this can be ensured by a proper selection of the lenses for this part.

---

[7]$18°\sim 0.314$ rad. Therefore $FOV = 200mm/50 \times 0.314$ rad $= 1.256$ mm for a symmetric system. With the chosen lenses the angle will be demagnified by a factor of 4, resulting in a FOV of 314 μm.

[8]$EP = 2 \times NA \times EFL$. Formula given on the manufacturer's website.

[9]The objective being apochromat, combined with its broad wavelength range, is an essential feature for acquiring widefield images of the samples under white light illumination 3.2, which was implemented during the building phase as it is essential for various phases of the construction.

[10]One of the main reasons this objective was chosen is actually its long working distance, allowing some space between the lens and the sample, needed in the future for poling the LiNbO$_3$ and imaging it at the same time.
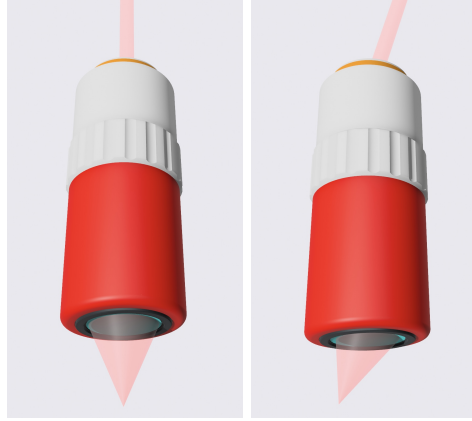
Figure 2.11: Non-deflected laser beam on the objective lens (left), deflected beam on the objective aperture (right), the PSF^2 will not have a circular distribution.

2.2 Estimation of the SHG power

In the case of a multiphoton microscope, specifically utilizing second-harmonic generation (SHG) imaging, the power of the pump laser plays a crucial role in the imaging process, as already explained. Multiphoton microscopy relies on the simultaneous interaction of multiple low-energy photons in lithium niobate, resulting in the emission of a higher-energy photon used for imaging. The pump laser, which provides the photons for excitation, determines the likelihood of multiphoton events occurring. Higher pump laser power leads to a more significant increase in photon density at the focal point, increasing the probability of multiphoton interactions and resulting in enhanced signal generation. Thus, a higher power pump laser allows for improved imaging sensitivity and better resolution, making it a vital parameter in optimizing the performance and capabilities of a multiphoton microscope using SHG. For this reason, a study of the power hitting the detector has been carried out prior to the building phase.

If one considers the excitation source as a plane wave (though this is not an exact representation of our specific case, as the power would be more concentrated in the case of a focused beam, making this a worst-case estimation), the power of the second harmonic generated light could be expressed using the formula provided by Gauderon in their 2001 work [6].

$$P_{2\omega} = \chi_2 \cdot \frac{P_\omega^2}{A} \cdot L^2 \cdot \frac{32\pi^3\omega^3}{c^3\epsilon(\omega)\sqrt{\epsilon(2\omega)}} \left(\frac{\sin\left(\Delta k L/2\right)}{\Delta k L/2} \right)^2 \tag{2.15}$$

where $P_{2\omega}$ is the power of the second harmonic signal, A is the area of the focused spot, L is the interaction length and $\Delta k = k_{2\omega} - 2k_\omega = \frac{4\pi}{\lambda}\left(n(2\omega) - n(\omega)\right)$. All the other values are known except for P_ω.

The temporal pulse can be modeled as a gaussian pulse modulated by our carrier sinusoid (Fig. 2.12):
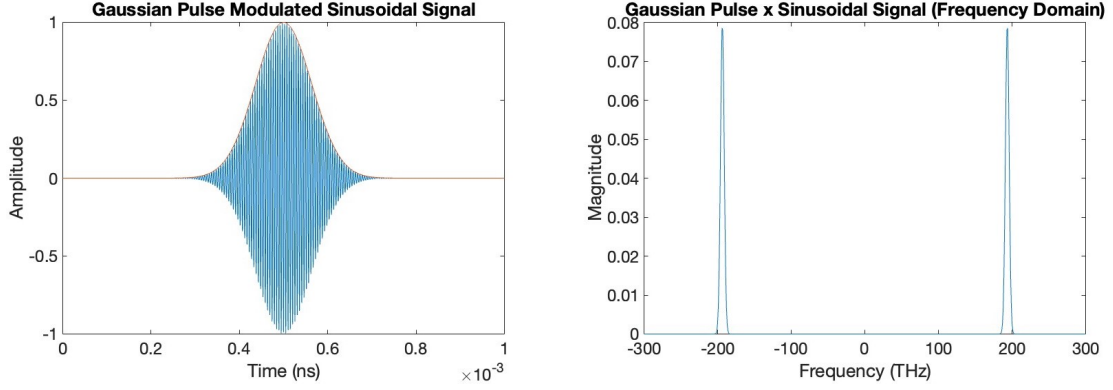
Figure 2.12: Gaussian pulse in the time domain (left) and spectrum (right).

$$E(t) = E_0 \exp\left(-\frac{t^2}{\tau_p^2}\right) \sin(2\pi f_0 t) = E_0 \exp\left(-\frac{t^2}{\tau_p^2}\right) \sin(\frac{2\pi \lambda_0 n(\omega)}{c}) \tag{2.16}$$

Let's now call $g(t) = E_0 \exp\left(-\frac{t^2}{\tau_P^2}\right)$ and $G(f)$ its Fourier transform, then:

$$E(f) = \frac{1}{2}G(f) * (\delta(f - f_0) - \delta(f + f_0)) = \frac{1}{2}\left(G(f - f_0) - G(f + f_0)\right) \tag{2.17}$$

Therefore its power spectral density will be equal to:

$$|E(f)|^2 = E(f)E^*(f) = \left[\frac{1}{2}\left(G(f - f_0) - G(f + f_0)\right)\right]\left[\frac{1}{2}\left(G^*(f - f_0) - G^*(f + f_0)\right)\right] \tag{2.18}$$

Neglecting the cross products, it is approximately equal to:

$$|E(f)|^2 \approx \frac{1}{4}|G(f - f_0)|^2 + \frac{1}{4}|G(f + f_0)|^2 \tag{2.19}$$

The power carried by the electromagnetic wave is given by the magnitude of the Poynting vector times the area of the surface over which the energy is flowing (A):

$$P(t) = A|\vec{S}(t)| = A\frac{E(t)B(t)}{\mu_0} = A\frac{E^2(t)}{c\mu_0} \tag{2.20}$$

From our laser specifications we know the laser's average power P_{avg} (using Parseval Theorem [12] and Poynting Theorem):

27

$$P_{\text{avg}} = \frac{1}{T}\int_{-\frac{T}{2}}^{\frac{T}{2}} P(t)dt = \frac{A}{Tc\mu_0}\int_{-\frac{T}{2}}^{\frac{T}{2}}|E(t)|^2\,dt = \frac{1}{Tc\mu_0}\int_{-\infty}^{+\infty}|E(t)|^2\,dt$$

$$= \frac{A}{Tc\mu_0}\int_{-\infty}^{+\infty}|E(f)|^2\,df$$

$$= \int_{-\infty}^{+\infty}\frac{A}{4Tc\mu_0}|G(f-f_0)|^2\,df + \int_{-\infty}^{+\infty}\frac{A}{4Tc\mu_0}|G(f-f_0)|^2\,df$$

$$= \frac{A}{2Tc\mu_0}\int_{-\infty}^{+\infty}|G(f)|^2 df = \frac{A}{2Tc\mu_0}\int_{-\infty}^{+\infty}|g(t)|^2 dt = \frac{A|E_0|^2}{2Tc\mu_0}\int_{-\infty}^{+\infty}|g'(t)|^2 dt, \quad g'(t) = \frac{g(t)}{E_0}$$

$$P_{\text{peak}} = P_{\text{avg}} \times \sqrt{\frac{2}{\pi}} \cdot \frac{T}{|\tau_p|}, \quad P_{\text{peak}} = \frac{A|E_0|^2}{2c\mu_0}$$

From here we can retrieve the peak power $P_{peak} = P_{avg}\frac{T}{\tau_p}\sqrt{\frac{2}{\pi}}$ (For instance $P_{peak} =$ 664.9038 W for 10 mW P_{avg}. The power will be attenuated by two mirrors (for beam walking, described in Sec. B.1) the galvo mirrors, scan lens, tube lens, dichroic mirror, and objective: Therefore, the actual peak power on the sample will be:

$$P_\omega = P_{peak} \cdot T_{mirror}^2 \cdot T_{galvo}^2 \cdot T_{scan} \cdot T_{tube} \cdot T_{dichroic} \cdot T_{objective} \qquad (2.21)$$

$T_{mirror} \sim 98\%$, $T_{galvo} \sim 98.1\%$, $T_{tube} \sim 87\%$, $T_{scan} \sim 93\%$, $T_{dichroic} \sim 98\%$, $T_{objective}$ not specified[11]. Now $P_{2\omega}$ can be computed as a function of P_ω. This is the second harmonic **peak** power generated in LN[12]. It will then be transmitted through the interface between LN and BOX and reflected back from the BOX-Si interface.

$$P_{objective} = P_{2\omega} \cdot T_{LN-BOX} \cdot R_{BOX-Si} \cdot T_{BOX-LN} \cdot T_{LN-air} \qquad (2.22)$$

$$R_{LN/BOX}^{2\omega} = \left|\frac{n_{LN} - n_{BOX}}{n_{LN} + n_{BOX}}\right|^2 = 0.0471 \quad R_{Si/BOX}^{2\omega} = \left|\frac{n_{Si} - n_{BOX}}{n_{Si} + n_{BOX}}\right|^2 = 0.1913 \qquad (2.23)$$

This power will then be multiplied by the transmission coefficient of the objective lens at $\frac{\lambda}{2}$, the reflection coefficient of the dichroic mirror, the transmission coefficient of the filter and the transmission coefficient of the collection lens:

$$T_{objective} = \text{unknown } R_{dichroic} = 99.5\%,\ T_{filter} = 98.2\%,\ T_{collection} \sim 97\% \qquad (2.24)$$

There is no detector that is able to follow the variations of signals in the range of fs (given the limits of the electronic components involved in the instrument[13]). Often, they

---

[11]The objective transmission is not specified anywhere but was then tested to be close to 99%.

[12]All the calculations shown in this section are implemented in the code in Sec. A.1.

[13]to follow the variations of 100 fs pulses, one would need electronics working at $\frac{1}{100\text{ fs}} = 10$ THz.

are not even fast enough to follow the repetition frequency. Therefore the peak power cannot actually be detected because the pulses get smoothened and the detector actually behaves as an average power detector. To understand that visually, the qualitative behavior has been simulated on MATLAB by filtering a signal with a LPF filter[14]. To
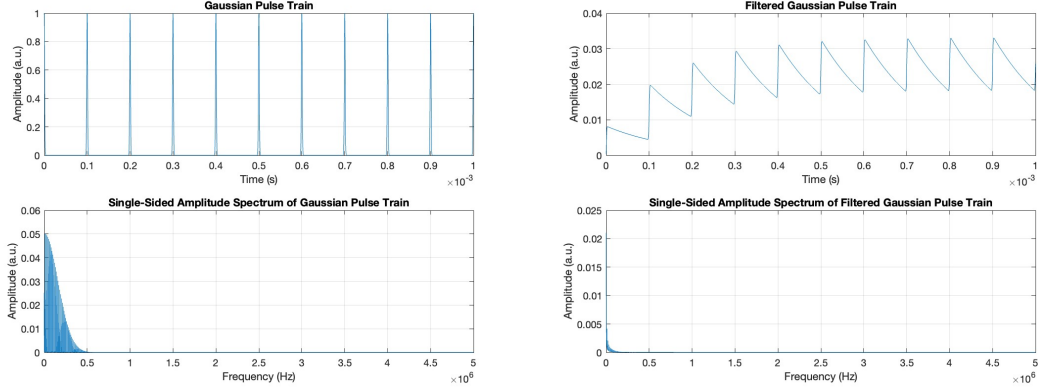

Figure 2.13: Time and frequency behavior of the pulses as they come out of the laser (left) and filtered by a Butterworth LPF (right). The signal stabilizes around the average value with small oscillations.

retrieve the average power knowing the peak power, the pulse width and the repetition period, the SHG pulses are assumed to be shaped just like the FH pump source[15]; so their average power can be calculated as:

$$P_{\text{avg}} = \frac{P_{\text{peak}}}{T} \sqrt{\frac{\pi}{2}} |\tau_p| \tag{2.25}$$

In order to assess the difficulty of the measurement, this power has been multiplied by the gain and sensitivities of commercially available detectors; an example is provided.

For THORlabs PMTs, the output voltage is given by the following formula:

$$Output(V) = TG(V/A) \times S(A/W) \times G \times OP(W) \tag{2.26}$$

where TG = Transimpedance Gain, S = Sensitivity, G = Gain and OP = Optical Power (hitting the sensor).

The most sensitive PMT for $\lambda = 775$ nm is PMT1001[16]: S = 55 mA/W, G = 3·10^6, TG = 11'000. This detector will output a voltage of 16.49 μV for an average SHG power of 9.09 fW, calculated through the script.

The PMT performances were compared to one of the APDs already available in the laboratory, and the results are described below. For APD440A the output voltage is given by:

---

[14]the frequencies have been scaled down to allow the computation.

[15]This assumption is not completely exact but is accurate enough for an order of magnitude estimation.

[16]its data can be found in the datasheet.

$$V_{\text{out}} = P_{\text{opt}} \times \Re_M(\lambda) \times G \qquad (2.27)$$

For the same average power of 9.09 fW, M = 100, a responsivity of 54 A/W, and a Transimpedance Gain G = 50 MV/A, the output voltage will be 24.54 μV, which is very similar to the PMT's output; for this reason, this detector was used.

Component	Part	Important Parameters
Laser	FSL1010	Wavelength: 1550 nm Power: 10 mW Pulse width: 150 fs Polarization: linear Rep. frequency: 80 MHz
Collimator	F240APC-1550	Function: Collimates light from fiber
Half-wave Plate	WPH05M-1550	Function: Rotates polarization along z-axis of LN
Dichroic Mirror	950 nm cut-on Longpass	Transmits: 1550 nm Reflects: 775 nm Cut-on: 950 nm
Shortpass Filter	FESH0900	Type: Shortpass Cutoff: 900 nm
Collection lens	LBF254-075	Function: Focuses light on detector
Tube lens	TL200-3P	f: 200 mm A_t: 47 mm λ range: [900 - 1900 nm]
Scan lens	SL50-3P	f: 50 mm A_t: 27 mm λ range: [800 - 1800 nm]
Scanning system	Galvanometric Scanner	Max scan speed: 30 kpps Max angle of deflection: 18°
Objective lens	MY50X-825	Back aperture: 3.36 mm Magnification: 50× λ range: [480 - 1800 nm] Working distance: 17.0 mm NA: 0.42
Detector	APD440A	Responsivity: 54 A/W G: 50 MV/A λ range: [400 - 1000 nm]

Table 2.2: Summary of Components. Block diagram in Fig. 2.1.

Chapter 3

Implementation

In this Chapter the practical aspects of the project are explored. This section provides a detailed guide on how the instrument was assembled and what are the main concerns during such an activity. This phase was not without its challenges. Unexpected issues were encountered that required the conduction of numerous experiments and adjustments to initial plans. From the initial setup to the fine-tuning of components, the entire process is outlined, including the hurdles faced and the solutions found. This chapter is crucial for understanding the physical aspects of the work and will be particularly useful for those interested in replicating the work or building upon it. By sharing these experiences, the aim is to equip future researchers with the knowledge to navigate similar challenges.

A new 3-dimensional version of the schematic view of the instrument was made (in Fig. 3.1 and 3.2) in order to give a more realistic perception of the final instrument and understand its operation; it is also divided in blocks (orange, blue, red and green) that will be explained in the following sections.

3.1 From the design to the real instrument

The general plan, as it can be understood from Fig. 3.1, is to build the setup on a breadboard, and keep it horizontal[1]. All the elements are placed in their position and held in place by optical posts, clamps and post holders, if necessary.

The first steps were devoted to figure out the size of the entire instrument and how to arrange the components on the breadboard in order to use the space in the most efficient way. So at the beginning only posts and clamps were placed on the breadboard to try to evaluate the needed space, like in Fig. 3.3.

After this evaluation, it became evident that a bigger breadboard was needed, so a new 30"×30" one was purchased. The following step involved ensuring that all the components were going to be aligned at the same height, in order to use the central part of the lenses, which is generally much higher in quality than the rest[2]. In order to perform

---

[1]The setup could also be put upright just by lifting the breadboard, in case of necessity.

[2]The only exception is that of the scan and tube lenses, whose full surface will be exploited. This is
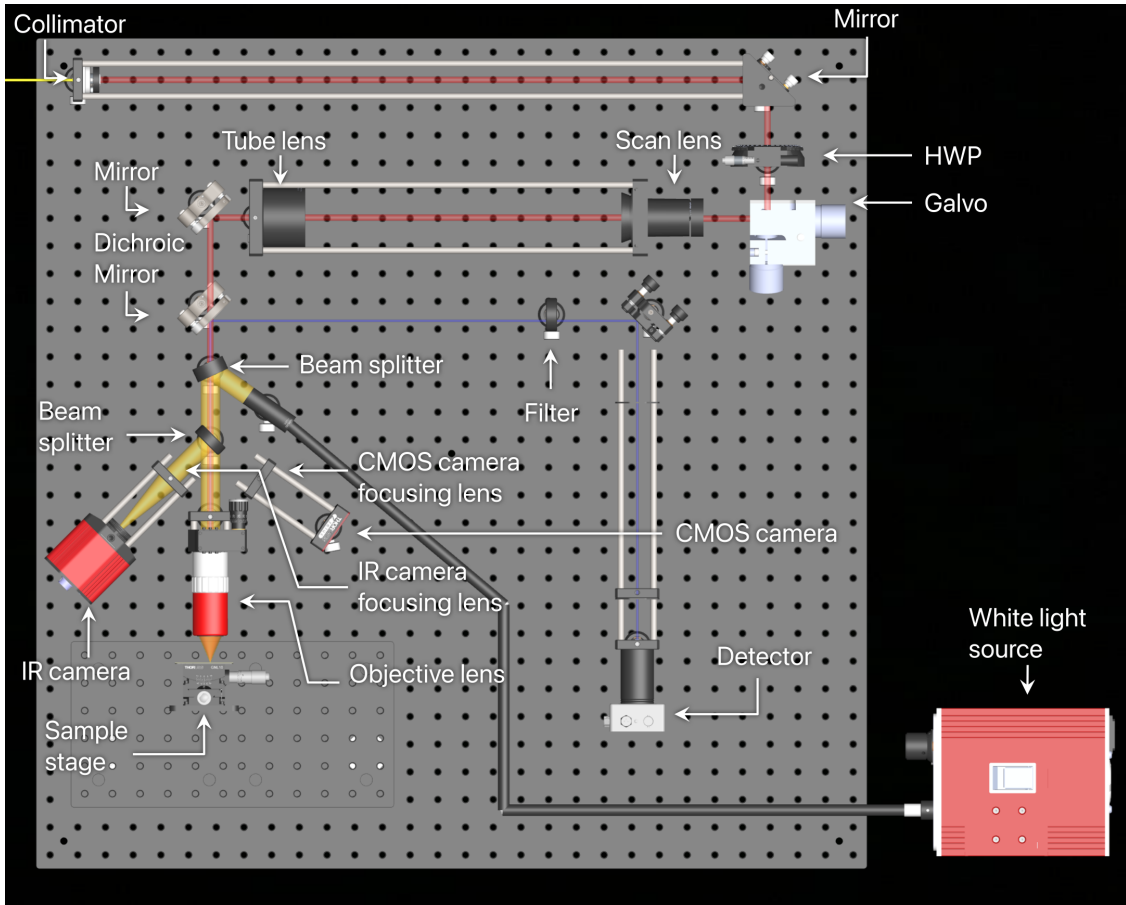
Figure 3.1: Complete schematic of the microscope, including what is needed to image the sample with white light (explained in Sec. 3.2).

a precise calculation prior to receiving all the components, it has been carried out on a CAD modeling software, leveraging the 3D models provided by the vendors (Fig. 3.4). Any differences in height given by components of different height were compensated by using spacers accordingly mounted on 1" posts (Fig. 3.5), or post holders and 1/2" posts (Fig. 3.2).

Several additional components were necessary in order to complete the instrument. Their function and usage will be listed and briefly described without going into detail because it is not the goal of this thesis (all the elements are shown in Fig. 3.1).

- KAD12F: A kinematic adjuster to correct the beam angle at the collimator, introducing a further degree of freedom in the alignment procedure.

- Cage plates and rods to favor a better alignment of the components, especially where the beam path is particularly long or in the case of the 4f system (Fig. 2.9),

---

the reason why they are much more expensive than standard lenses.
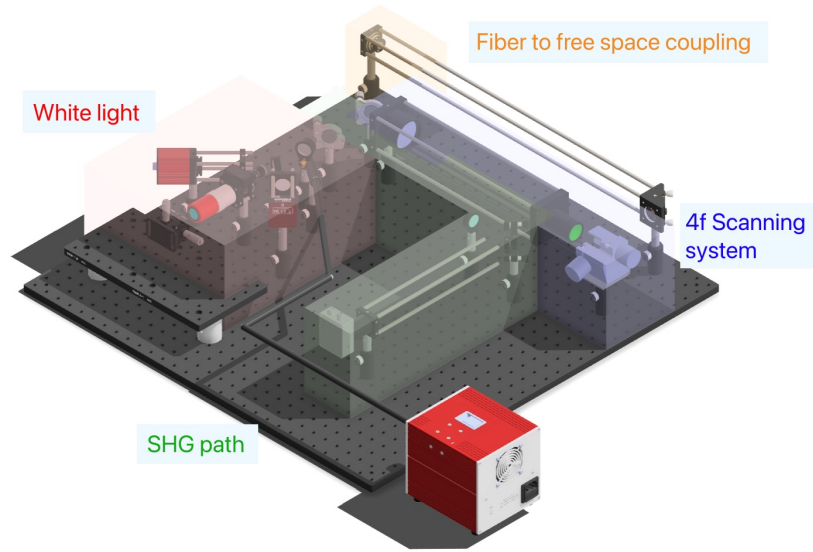
Figure 3.2: Final version of the instrument divided into 4 blocks that will be described in this section.
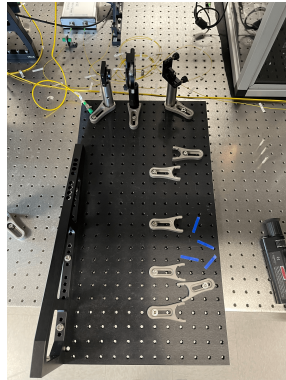
Figure 3.3: Size evaluation of the instrument.

where the distances had to be well calibrated in order to have the desired beam characteristics (better discussed in Sec. 3.4).

- Beam splitters and a white light source to allow widefield imaging of the sample under white light or IR (see 3.2) and SHG at the same time.

- A Z-control on the objective lens to focus the light on the sample.

- A sample holder to host the chips to be imaged.

- A manual stage to move the chip on x and y axes and center the light on the desired ROI.

Figure 3.4: Evaluation of the height differences using a CAD software.
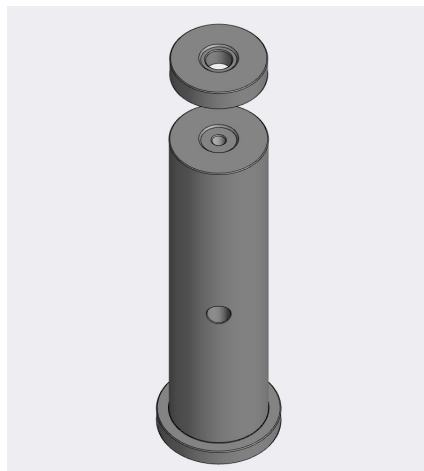
Figure 3.5: A post spacer is used to adjust the height of a post to align all the components on the same height.

After understanding the dimensions of the system the first parts were placed on the breadboard (Fig. 3.6).

3.2 Widefield white light imaging

After the initial phases of the implementation stage it was immediately clear that a white light source had to be introduced to image the samples in a widefield fashion in order to be able to see where the 1550 nm laser was being focused. In order to introduce
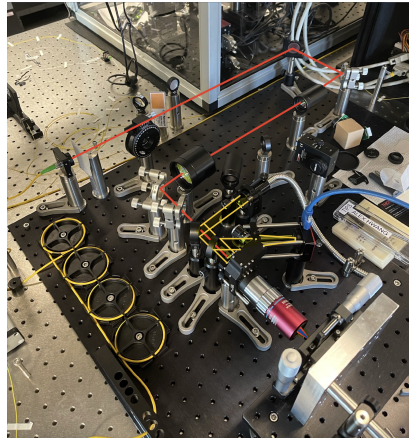
Figure 3.6: First version of the microscope mounted on the optical table. The laser path is sketched in red.

this capability in the already designed instrument, 2 beam splitters are needed and were inserted as shown in Fig. 3.1 and 3.7. A white light source, namely OSL2, produces a white spectrum of light in the range [300 nm - 1800 nm]. The light is coupled into a fiber and transported near the objective lens. At this point, the light coming out of the fiber is highly divergent, and so not suited to create an image; for this reason it is collimated by means of a collimator (OSL2COL[3]), which brings the divergence down to acceptable values. The light gets then partially reflected through a 50-50 non-polarized beam splitter and partially lost. The reflected light will then get split again. The transmitted part is the relevant one and will hit the objective back aperture and get focused on the sample. The chosen imaging configuration is epi-illumination, to be able to image samples with reflective substrates. Therefore the light is focused by the objective lens onto the sample and reflected back, to be collected by the same objective lens. The light propagating back from the objective aperture will be collimated, as MY50X-825 is an infinity-corrected objective. Infinity-corrected objectives are a type of optical system used primarily in microscopy. Unlike finite corrected objectives, which produce a real image at a fixed distance from the objective, infinity-corrected objectives produce an image at an infinite distance. This allows for the insertion of additional optical components, such as beam splitters (like in our case) or filters, in the optical path without altering the image focus. For this reason, this objective needs a tube lens to focus the light on the detector (the camera sensor in our case). Since the image does not need to be highly qualitative, because this channel of the microscope will be only used to estimate what part of the chip is being investigated by the laser light, any lens does the job, and there was no need to buy more expensive and fancy tube lenses. The choice was to use a LA1509, a plano-convex lens with f = 100 mm, to achieve an acceptable magnification. The magnification given by this optical system consisting of an infinity-corrected objective lens and a tube

---

[3]OSLCOL was actually purchased after the first images to enhance the quality. In the first acquisitions another collimator was used, whose lens quality and collimation were inferior.

lens can be assessed through the following formula:

$$\text{Magnification} = \text{Design Magnification} \times \frac{f_{\text{Tube Lens in Microscope}} \text{ (mm)}}{f_{\text{Design Tube Lens of Objective}} \text{ (mm)}} \qquad (3.1)$$

Since the design tube lens focal length is 200 mm, in our case the magnification will be $25\times$. The camera used to capture images is a Zelux® 1.6 MP Color CMOS Camera; its sensor area is quite large and therefore the alignment was not hard to achieve.
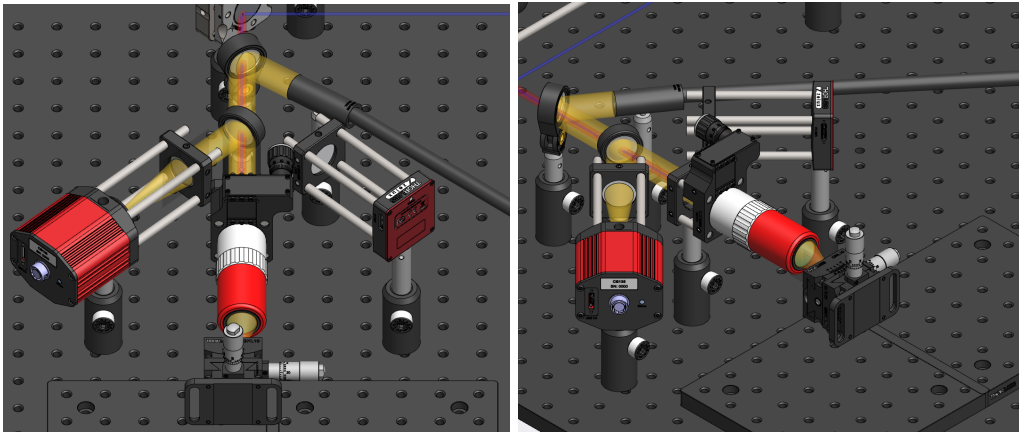
Figure 3.7: White light imaging path of the microscope. In this representation, the light is actually focused on the IR camera, discussed in 3.2.1.

The first attempts to verify the correct behavior of this part of the imaging system were invested in taking an image of a metallic post, with another lens, that was the only one available at that moment (a f = 40 mm lens) (Fig. 3.8).

The first image was blurry, not well centered, and was suffering from a secondary overlapping image given by some stray reflection in the optical system. This was fixed by correcting the focus and alignment, and using the opposite side of the second beam splitter. After solving that issue and removing the filter, the 75 mm lens that was intended to be used, was mounted in the setup and the image looked like in Fig. 3.9.
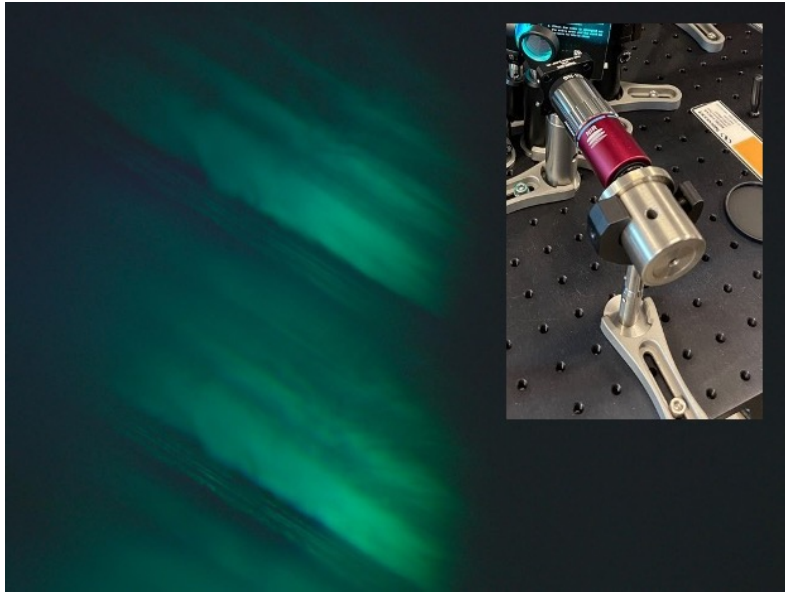
Figure 3.8: Image of a metallic post. The image appears blueish because a filter has been applied to cut off 775 nm and 1550 nm light from the white light source to not have involvement of this light on the sample. It will be later proved as unnecessary.
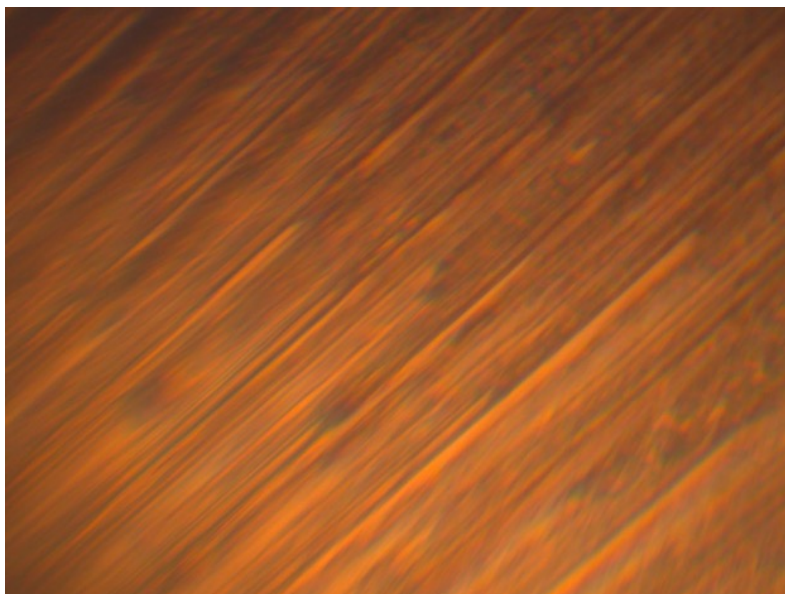
Figure 3.9: Utilizing a 75 mm lens for enhanced magnification and detail capture on the camera.

After these first tests, confirming that the microscope was behaving as expected, the first images of the chips were acquired through the instrument (Fig. 3.10).

37
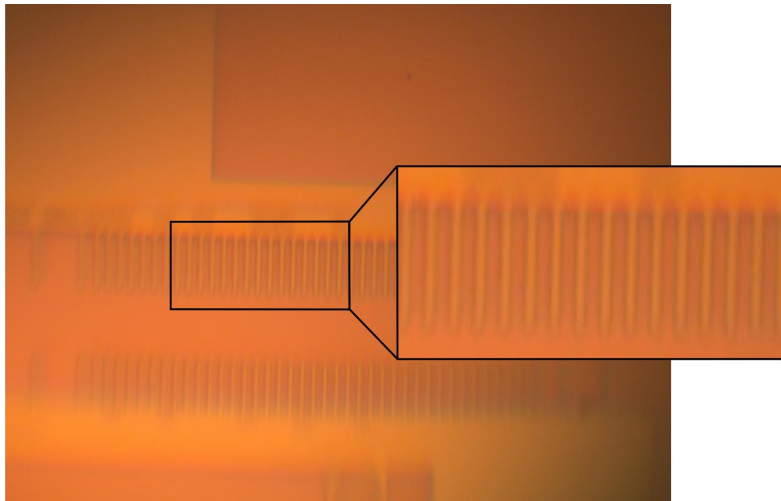
Figure 3.10: Chips imaged through white light.

Reattaching the filter to reduce chromatic aberration resulted in a decline in overall image quality, so it was not used in the final setup (Fig. 3.11).
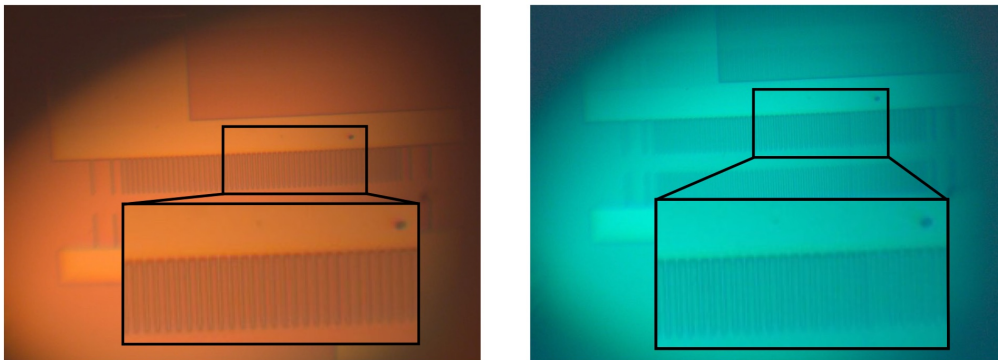
Figure 3.11: Comparison between two images: one was acquired with the filter attached and the other one without.

After further adjustments (improved alignment, precision focusing due to the introduction of the Z-control discussed in 3.1, and optimal lighting), the image quality obtained is that in Fig. 3.12.

38
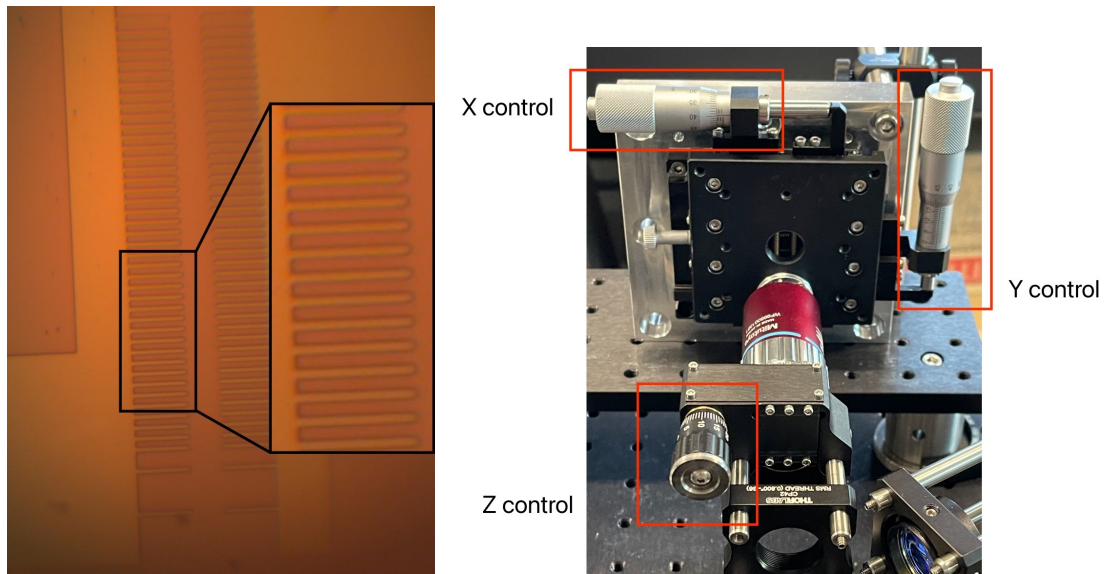
Figure 3.12: Final image quality on the left, obtained through the construction on the right.

The new collimator provided a better image quality (less distortion at the edges) at the cost of an image with some black parts due to the dirty interior lenses, that couldn't be cleaned (Fig. 3.13).
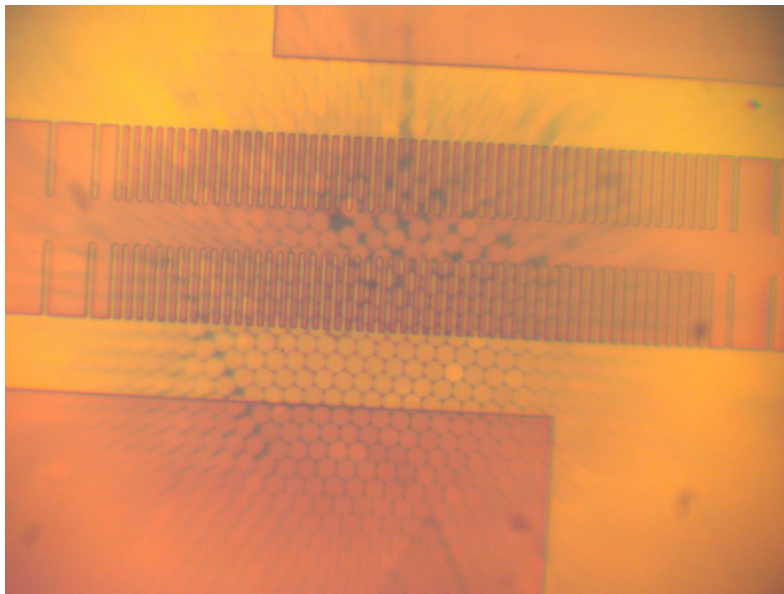
Figure 3.13: Final image quality with the new collimator.

3.2.1   IR imaging

Imaging the samples under IR light was extremely important during the setup of the scanning system because it allowed to see the 1550 nm laser spot on the chip, bringing several advantages:

- Obtaining a correct alignment of the laser beam on the objective lens[4].

- Assess the functionality of the scanning mechanism (by comparing the movement of the spot to the expected behavior).

- Correctly focus the laser beam[5]

The light source used is the same (as the emission spectrum includes a significant part of the IR range), and the working principle is exactly the same as for the standard white light part. The lens used to focus light onto the camera sensor is LBF254-075, a form lens with a focal length of 75 mm, providing a magnification of $18.75\times$. The IR camera is SenS SWIR 640V-ST/STP, and it is not equipped with a CMOS sensor, but rather with a InGaAs sensor, more sensitive in the IR range. The quality provided by this channel of the microscope is inferior to the white light one, because of the technological limitations of the sensor: IR cameras can be expensive due to the materials and technology and usually provide an overall worse quality image. In addition, the wavelength used to acquire the image is longer, leading to a limited resolution (see Eq. 2.2). The best quality of IR images that can be taken with the Swir camera is shown in Fig. 3.14.

---

[4]When changing the focus the Airy disks stay circular if the laser is hitting the objective back aperture in a perpendicular direction.

[5]As discussed in 3.4, aligning the 4f system with the correct distances between the different lenses is not an easy task, therefore having visual feedback on the collimation of the beam is extremely useful. It can be assessed by changing the distance between the lenses until the laser is perfectly focused when the image is crisp (being MY50X-825 an apochromat objective and the light forming the image well collimated).
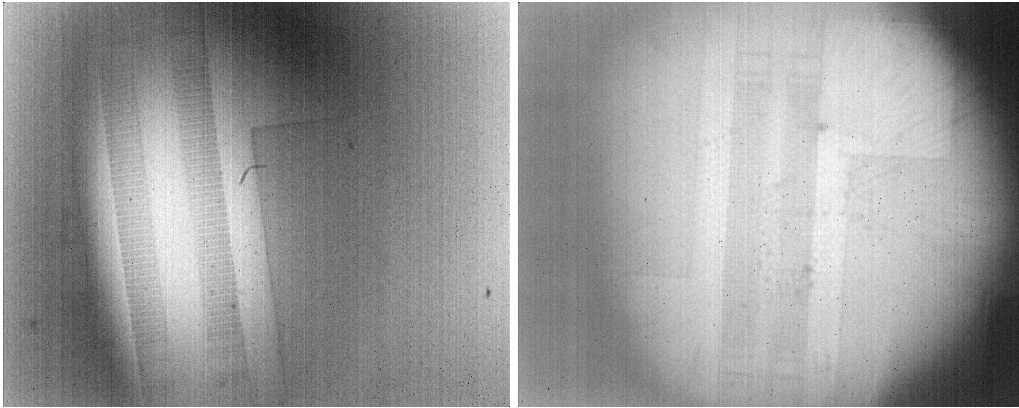
Figure 3.14: IR image with the old white light collimator (left) and with the new one (right). In this case, the image quality is definitely superior to the old collimator because some image processing algorithms are applied to the image to sharpen the edges. They couldn't be applied to the second image because of the disturbances introduced by the dirt, which produces an even worse result. Nonetheless, the resolution is not as relevant in this case, because the camera was mainly used for the previously listed reasons.

3.3 Fiber to free space coupling (Pulse dispersion)
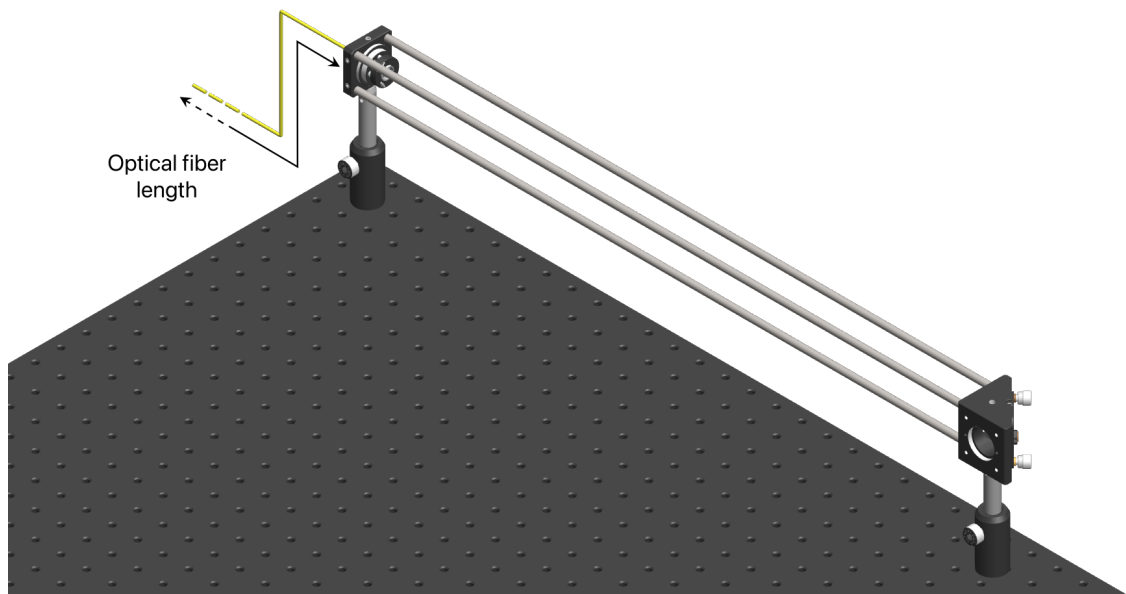
Figure 3.15: The picture shows the final part of the optical fiber going from the laser to the collimator, the collimator itself and a mirorr.

This part of the setup (Fig. 3.15) has the role of coupling light from the fiber laser into free space in a collimated beam. To achieve this, light is first transported through a 4

m long single-mode fiber cable from the FSL1010 output to the collimator. At its output, light is not divergent anymore and can be easily directed towards the rest of the apparatus steering the beam with mirrors. The process of transporting light through fiber does not come without drawbacks: pulse dispersion in fiber optics is a phenomenon where light pulses spread out as they travel through an optical fiber, leading to a reduction in peak power. This dispersion can be attributed to various factors such as the differing speeds of light rays, modal properties, and material characteristics of the fiber. Understanding and mitigating pulse dispersion has been critical for the optimization of the system, because, as described in Chap. 2, the SHG power scales quadratically with the FH peak power. Therefore, a 10 times enlargement of the pulse width leads to a 10 times lower peak power and thus to a 100 times lower SHG power, which is much harder to detect. To understand what happens to the pulse when it travels through optical fiber, a summary of what is explained in [2] is reported. To calculate the dispersion, we can start considering Eq. 3.2, describing the propagation of a pulse envelope $A(z, \eta)$ in a dispersive medium along the z-direction:

$$i\frac{\partial A}{\partial z} = -\frac{i\alpha}{2}A + \frac{\beta_2}{2}\frac{\partial^2 A}{\partial T^2} - \gamma|A|^2 A \tag{3.2}$$

The first term of the right-hand side accounts for the fiber losses, the second term for dispersion and the third term for nonlinearity. While nonlinearity or dispersion can dominate over the other, losses are always present. To take them into account the normalized amplitude $U(z, \tau)$ can be defined as:

$$A(z, \tau) = \sqrt{P_0}\exp(-\alpha z/2)U(z, \tau) \tag{3.3}$$

where τ is defined as: $\tau = \frac{T}{T_0} = \frac{t - z/v_g}{T_0}$ and P_0 is the pulse's peak power. Therefore, the exponential term allows including the losses inside $U(z, \tau)$.

Let's now analyze the case where dispersion is prevalent; the propagation equation 3.2 becomes 3.4:

$$i\frac{\partial U}{\partial z} = \frac{\beta_2}{2}\frac{\partial^2 U}{\partial T^2} \tag{3.4}$$

The symbol T represents a shifted time variable ($T = t - z/v_g$), to be in the frame of reference of the pulse (it basically moves along the propagation direction with the group velocity of the envelope).

An easy way to solve this equation is switching to the frequency domain. We can consider $\widetilde{U}(z, \omega)$, the Fourier transform of $U(z, T)$ calculated as:

$$U(z, T) = \frac{1}{2\pi}\int_{-\infty}^{\infty}\tilde{U}(z, \omega)\exp(-i\omega T)d\omega \tag{3.5}$$

and rewrite[6] 3.4 as:

$$i\frac{\partial \widetilde{U}}{\partial z} = -\frac{1}{2}\beta_2\omega^2\widetilde{U}. \tag{3.6}$$

---

[6]derivation with respect to time corresponds to multiplying by $i\omega$ in the frequency domain.

The general solution of this differential equation is:

$$\tilde{U}(z,\omega) = \tilde{U}(0,\omega)\exp\left(\frac{i}{2}\beta_2\omega^2 z\right). \tag{3.7}$$

Plugging 3.7 into 3.5, leads to the solution in time domain:

$$U(z,T) = \frac{1}{2\pi}\int_{-\infty}^{\infty}\tilde{U}(0,\omega)\exp\left(\frac{i}{2}\beta_2\omega^2 z - i\omega T\right)d\omega \tag{3.8}$$

where $\tilde{U}(0,\omega)$ is the Fourier transform of the field at the input (Eq. 3.9):

$$\tilde{U}(0,\omega) = \int_{-\infty}^{\infty}U(0,T)\exp(i\omega T)dT \tag{3.9}$$

In the case of a Gaussian pulse (that is actually our case), the input envelope is of the form:

$$U(0,T) = \exp\left(-\frac{T^2}{2T_0^2}\right). \tag{3.10}$$

We can then calculate the general solution Fourier transforming the pulse (Eq. 3.9) and then integrating it according to Eq. 3.8. The solution is:

$$U(z,T) = \frac{T_0}{\left(T_0^2 - i\beta_2 z\right)^{1/2}}\exp\left[-\frac{T^2}{2\left(T_0^2 - i\beta_2 z\right)}\right] \tag{3.11}$$

and it shows that a Gaussian pulse at the input stays a Gaussian pulse, but the pulse width T_0 increases with propagation, following the relation (eq. 3.12).

$$\frac{T(z)}{T_0} = \sqrt{1 + \left(\frac{z}{z_D}\right)^2} \Rightarrow T(z) = T_0 \cdot \sqrt{1 + \left(\frac{z}{z_D}\right)^2} \tag{3.12}$$

z_D is called dispersion length and it is defined as $T_0/|\beta''|$.

Sometimes the dispersion is characterized by manufacturers by means of D, which is directly proportional to β'':

$$D\left[\frac{ps}{nm \cdot km}\right] = \frac{2\pi c}{\lambda^2}\beta'' \tag{3.13}$$

From this document we can retrieve information about SMF-28, the optical fiber that was used to transport the laser beam from the FSL1010 laser to the input of the setup.

The document states that the parameter D is less than $18\ \frac{ps}{nm \cdot km}$. By substituting this value into Eq. 3.13, we arrive at a value of $\beta'' = 23.000\ fs^2/m$, from which the dispersion length $z_D = 0.4891$ m can be derived. This then enables us to calculate the relative pulse dilation $\frac{T(z)}{T_0}$ as a function of the normalized length $\frac{z}{z_D}$, and subsequently, the pulse width at the fiber's output (Fig. 3.16).

With a 12-meter-long cable, like the one initially used, the pulse width was broadened to over 3 ps. This necessitated a rearrangement of the setup, allowing the laser to be positioned closer to the microscope. By using a 4-meter-long fiber, the pulse was reduced

to 1.2 ps. Utilizing the MATLAB script that was previously employed for the SHG power calculation, and setting the pulse width to 1200 fs = 1.2 ps, we obtained a power on the detector equal to 1.14 fW.
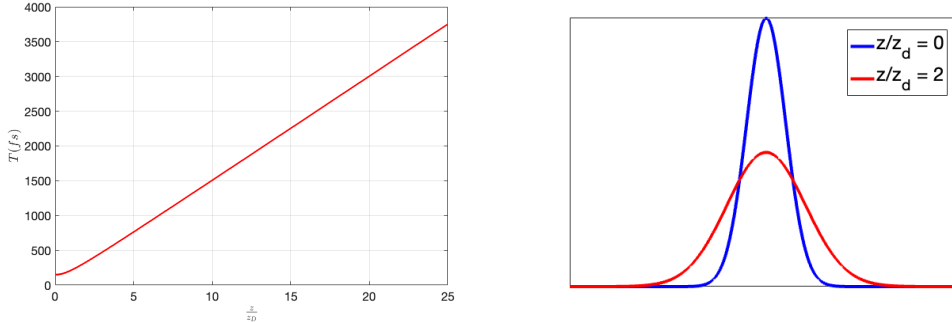
Figure 3.16: Pulse width as a function of the normalized length z/z_D, with $T_0 = 150$ fs (left).
Broadened pulse (right).

3.4   4f-like scanning system

A 4f-system, often used in optics and photonics, is a type of imaging system that consists of two lenses. The name "4f" comes from the arrangement of these lenses: the first lens (with focal length f) is placed at a distance f from the object, and the second lens is placed at a distance 2f from the first lens, with the image formed at a distance f from the second lens. Hence, the total length of the system is 4f. This configuration is particularly useful because it performs a Fourier transform of the object's spatial distribution at the plane halfway between the two lenses, allowing for spatial filtering and phase manipulation (like in Zernike configuration). The 4f system is a fundamental building block in many optical systems, including microscopes, but in our case its goal is just to manipulate the angle of incidence of light on the objective without altering the position hit by the beam (illustrated in Fig. 3.18).

In the scanning system, the two lenses are typically referred to as the scan lens and the tube lens. The scan lens, positioned first in the system, is responsible for focusing the light from the laser source and directing it toward the tube lens. This lens is crucial in determining the angle of incidence of the light on the objective. The tube lens, on the other hand, is responsible for collimating the diverging light from the scan lens and directing it towards the objective lens, which will focus it onto the image plane. This lens plays a significant role in maintaining the position hit by the beam, ensuring that the light is focused precisely where it is needed. Both lenses work together to manipulate the light's path without altering its destination, making this 4f-like system a versatile tool in optical and photonic applications.
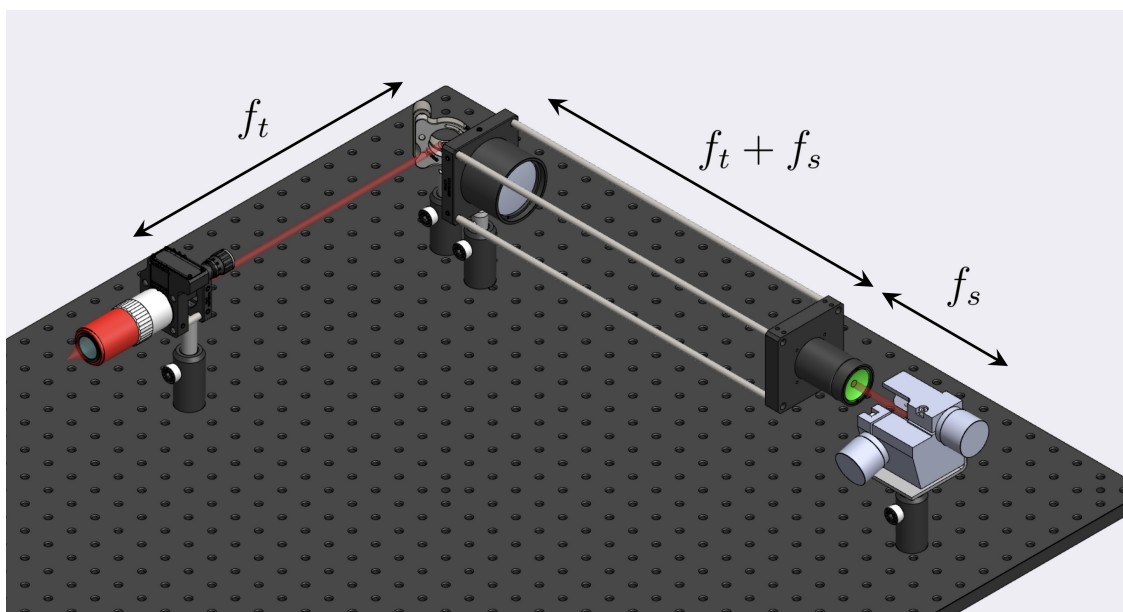
Figure 3.17: 4f system with the appropriate distances between the lenses
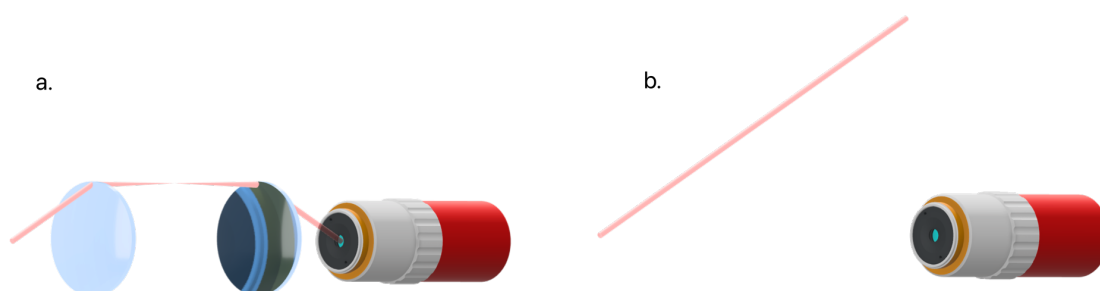
Figure 3.18: In a. the laser beam is deflected by a certain angle, and the system of lenses makes sure that the beam will hit the center of the objective aperture with the same angle without getting off-centered. In b. the laser beam is deflected but it cannot hit the right spot.

3.4.1 Scan & Tube lenses

The alignment of the scan and tube lenses is crucial and must therefore be performed with the maximum precision, otherwise the scanning will result to be imprecise and the beam may be not correctly focused on the sample (leading to an asymmetric PSF[2], due to a not perpendicular angle of incidence of the laser light on the back aperture). To achieve this goal, a cage system has been used, in order to position the lenses at the design distance with a very low error. Even though in the design phase the lenses were

considered as "thin lenses[7]", the real lenses that are used in the setup do have a thickness, and in many cases it is not negligible at all because they consist of many lenses, like in the case of TL200-3P and SL50-3P; for this reason it is not possible to place them and choose their relative distance only knowing information about their focal lengths in Figs. 3.17 and 2.7. For this kind of lenses it is necessary to know other parameters, that are explained below. For the scan lens, it is specified that (see Fig. 3.19 for reference) the scanning distance is 37.8 ± 4 mm, the working distance is 26.4 mm and the parfocal distance is equal to 77.3 mm.
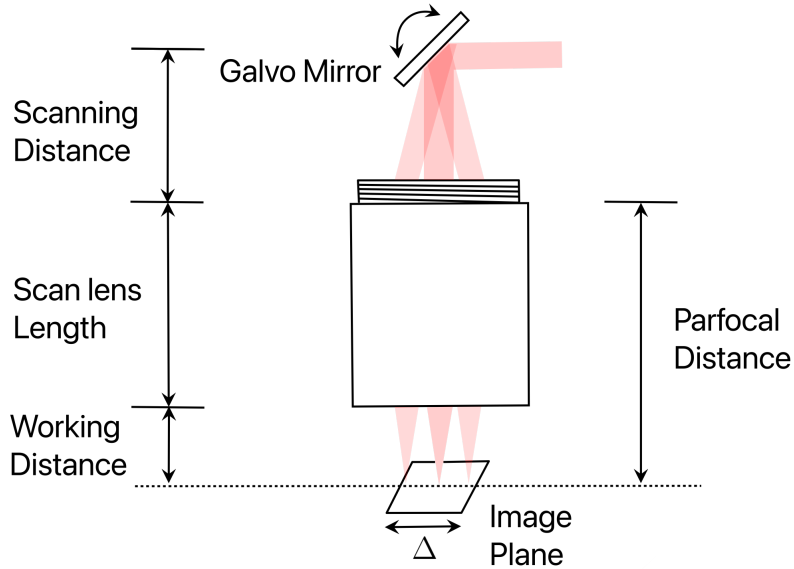
Figure 3.19: This schematic illustrates the role of the scan lens and its essential parameters. The **scanning distance** refers to the required distance between the galvo mirror and the scan lens's aperture, replacing the f_s value in Figs. 3.17 and 2.7. Following the objective lens, the **working distance** is defined as the separation between the scan lens's extremity and the image plane. This provides a more accurate representation of the f_s contribution to the $f_s + f_t$ distance in Figs. 3.17 and 2.7. The **parfocal distance** may also serve the same function. Δ represents the same displacement as seen in Figs. 3.17 and 2.7.

The light focused by the scan lens is collected by the tube lens at a significant distance from the image plane (Fig. 3.20), where it is highly divergent. To properly collimate the light and calibrate the appropriate distance between the lenses, the working distances of both the scan lens and the tube lens (180.9 mm) were summed. This calculation was used to determine the optimal positioning of the two optical elements. Finally, the objective lens position was chosen to be 189.1 mm away from the tube lens housing, i.e. the pupil distance.

The resulting system is shown in Fig. 3.22 and at this stage of the project was ready

---

[7]The approximation of thin lenses is well explained in [11].
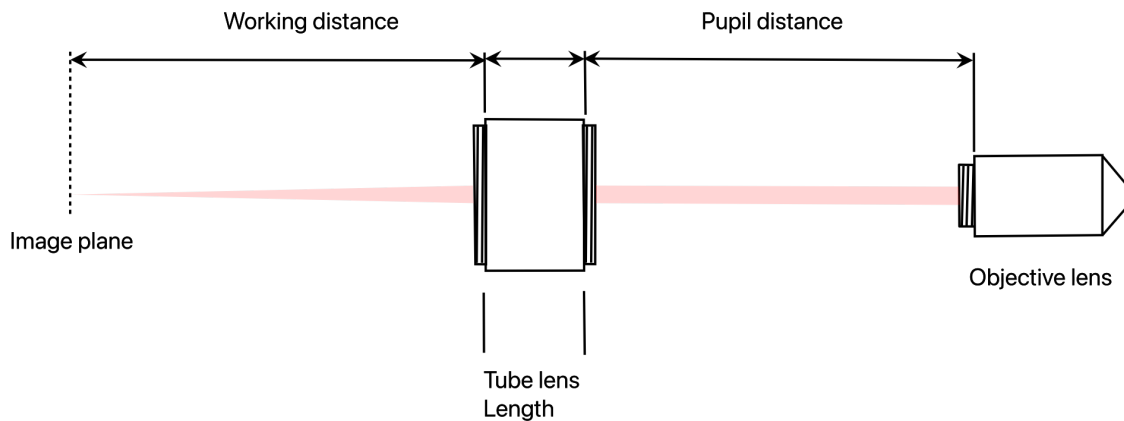
Figure 3.20: The same schematic was made for the objective lens. The **working distance** has the same meaning as for the scan lens. The only other parameter is the **pupil distance**, that is to say the distance between the extremity of the tube lens housing and the entrance pupil of the objective lens.

to be tested. The first tests were conducted manually by tilting the beam instead of using the galvanometric scanner directly, in order to assess the correct behavior of the system without introducing other possible sources of errors. For this reason, a silver mirror has been mounted on a Polaris mirror mount that allowed a fine and precise tilting of the former. The mirror mount was placed at a scanning distance from the scan lens, just as if it was the actual galvo.

This part of the setup turned out to be functional and the laser spot (imaged through the IR camera) could be moved across the sample thanks to the knobs (3.21).

3.4.2   Galvanometric scanner

This section will briefly explain how a galvanometric scanner works in the context of microscopy. The device's role in scanning samples is essential, and understanding its operation can offer valuable insights.

The galvanometric scanner consists of 2 main components: **galvanometer motors** and **mirrors**; the motors control the deflection of the laser beam along the x and y axes, rotating the mirrors, that are precisely attached to the galvanometer motors, as depicted in the model of Fig. 3.23.
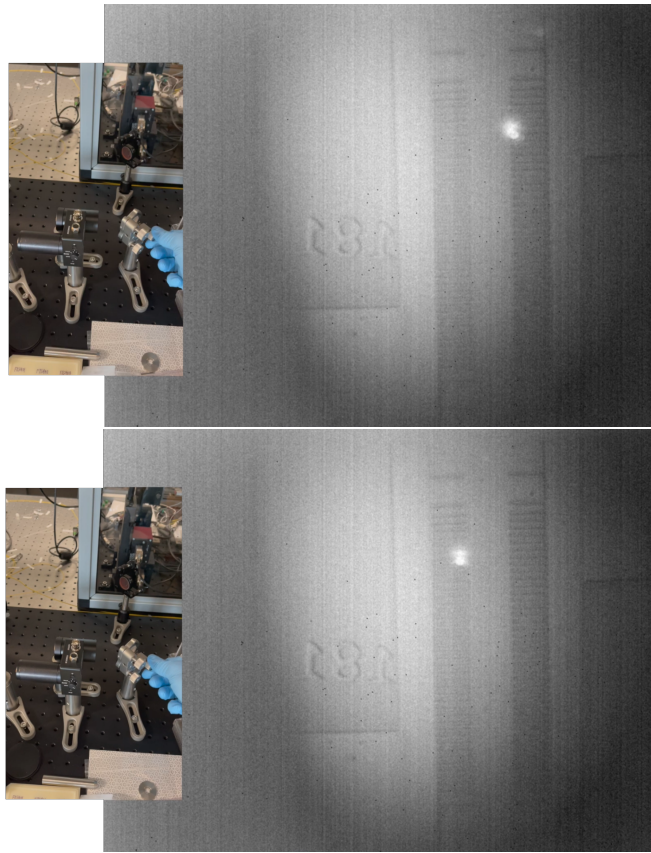
Figure 3.21: Final results of the 4f system alignment
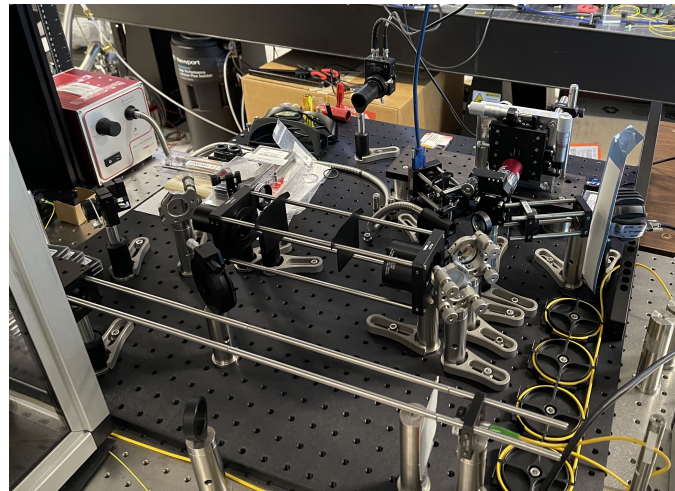
Figure 3.22: Picture of the scan system implemented. A schematic view (in a 1:1 scale), is represented in Fig. 3.17.
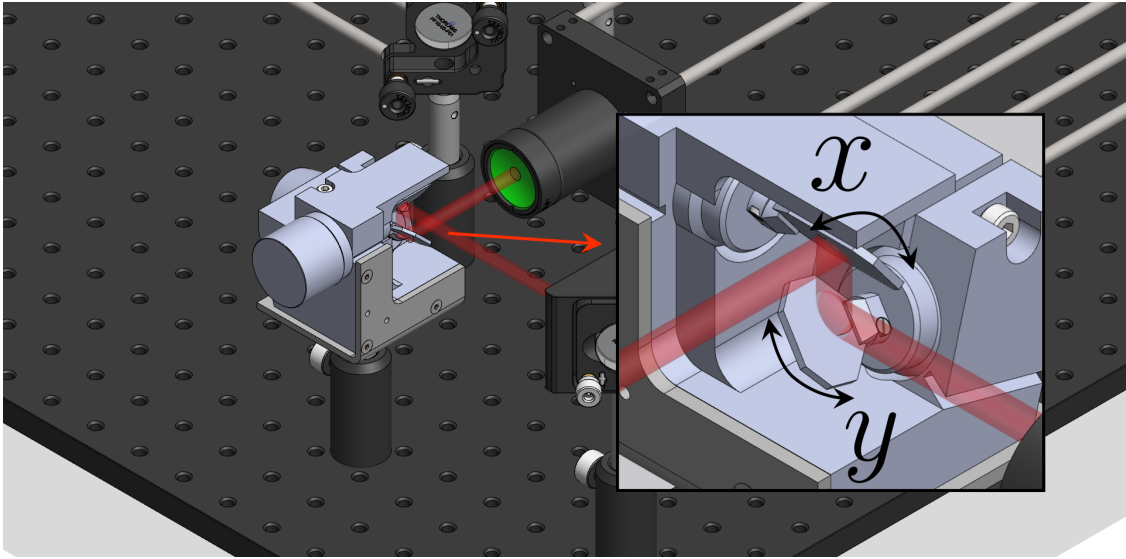
Figure 3.23: Galvanometric scanner.

Working Principle:

1. **Deflection on the X-Axis**: The laser beam's horizontal movement is controlled by the first galvanometer motor. By finely adjusting the mirror's angle, the beam scans the sample from left to right along the x-axis.

2. **Deflection on the Y-Axis**: The vertical scanning is managed by the second galvanometer motor. It alters the mirror's angle, moving the laser beam up or down along the y-axis, enabling a complete vertical scan of the sample.

3. **Combined Movement for Scanning**: By synchronizing the control of both motors, the laser beam can be directed to any point in the x-y plane. This coordinated movement allows for a comprehensive and detailed scanning of the sample, creating a complete image of the area under examination. The methodology used in our implementation is of raster scanning the surface, therefore one motor will move at a frequency that is lower than the frequency of the other one by a factor equal to the number of rows (or columns) that one desires the image to be composed of. The frame rate will be dictated by the slower motor.

Combination with scan & tube lenses   The galvo alone is sufficient to scan surfaces, without the need for other optical components, although it is only suitable to scan macroscopic surfaces; to tackle this issue one can couple it to a lens, that will transform the different angles of incidence into different positions on the sample (Fig. 2.8). In order to achieve an adequate resolution it is mandatory to use an objective lens, which is characterized by a high NA, but objective lenses usually also have a narrow back aperture, and therefore the deflection angles that could be "accepted" by the lens would be limited to very small ones, leading to an extremely narrow FOV on the sample; for this reason, as

already described in Sec. 2.1.7, a total of 2 lenses (scan and tube) are utilized, allowing to get a very high resolution and the scanning of a reasonable portion of the sample.

Returning to the subject of the practical implementation of what was described, two steps were performed to adapt the scanner to the setup:

- Measure the reflectivity of the provided mirrors at 1550 nm

- Understand the type of signal that the galvo motors needed to work

Galvo mirrors

The purchased galvo primary use is deflecting visible light, therefore its reflectivity was measured to understand if the mirrors were suitable to steer a 1550 nm laser.

The results are reported in Fig. 3.24. The measurement was not easy to perform because the laser is invisible to the naked eye and not even detector cards can be used below a certain power to individuate the laser beam. For this reason, the detector was continuously moved around the area where the laser was expected to be found until an increase in the signal was observed; at that point, it was immobilized in the best possible way in order to maximize the signal with successive movements. There is a clear saturation value for all the different measurements, that slightly differs between each of them due to the different angle of arrival on the detector, because of the inevitable imprecise nature of the positioning process during the measurement. That saturation value never went above 0.75 mW, which suggested that the mirrors were not suited for IR.
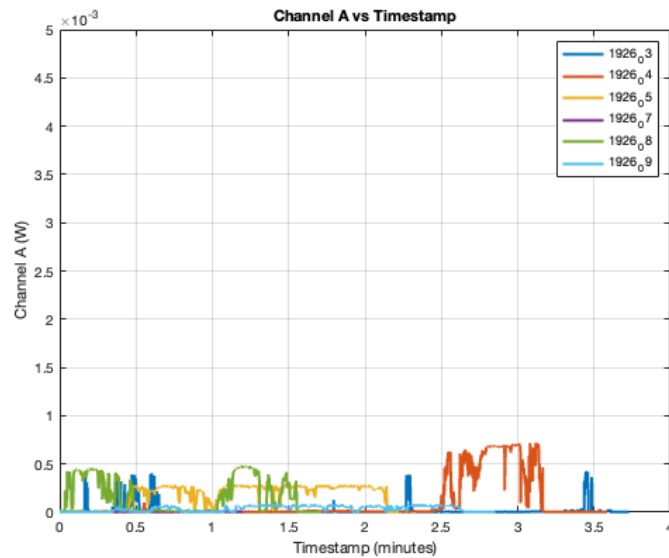
Figure 3.24: Power measurements of the reflected light. On the x-axis is time, and on the y-axis is reflected power.

Two consecutive solutions were adopted to overcome this problem, both relying on

choosing a different material for the mirrors. The choice was made among the available materials and the ones with a large reflectivity around 1550 nm.
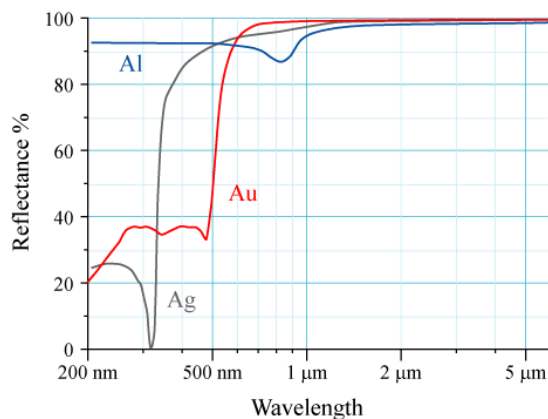
Figure 3.25: Reflectivity spectrum for Al, Ag and Au.

As a first attempt, **Al was deposited on kapton tape**, a polyimide film that is used in a wide variety of applications, particularly where a thin, durable tape that can withstand high temperatures is required; in our case, it was selected because of its lightweight (to not affect the galvo resonant motors) and particularly smooth surface. The polyimide film that makes up the tape is manufactured to have a uniform and consistent surface, which is especially useful if one wants to use it as a substrate for a deposition, and then use the resulting surface as a mirror. The kapton tape has been fixed to the evaporator chuck thanks to the clamps and then got a 500 nm layer of Al evaporated on (Fig. 3.26). The best part of the tape (in terms of rugosity and uniformity) was cut out and transferred on the galvo motor (right image in Fig. 3.26) and then the excess was removed.

This first methodology brought to a great increase of the reflectivity, as expected, but also to a deterioration of the beam spot shape, and stray reflections (Fig. 3.27). This denotes an insufficient quality of the kapton tape as a substrate for deposition for optical purposes.

The second attempt consisted of **fabricating new gold mirrors** to be attached to the ones already on the scanner.

The process consisted of a few steps, after depositing a 200 nm thick layer of Au on a 350 um thick silicon wafer:

1. Spin coating: the wafer surface was protected by a resist, to prevent particles and dust from getting on the surface of the newly deposited gold during the cleavage.

2. Cleavage: the wafer has subsequently been cleaved, in order to have mirrors of the same size of the old ones.

3. Resist removal: after cleaving the chips, they were submerged in a solution of acetone and IPA that got rid of the resist and exposed the highly reflective gold surface.
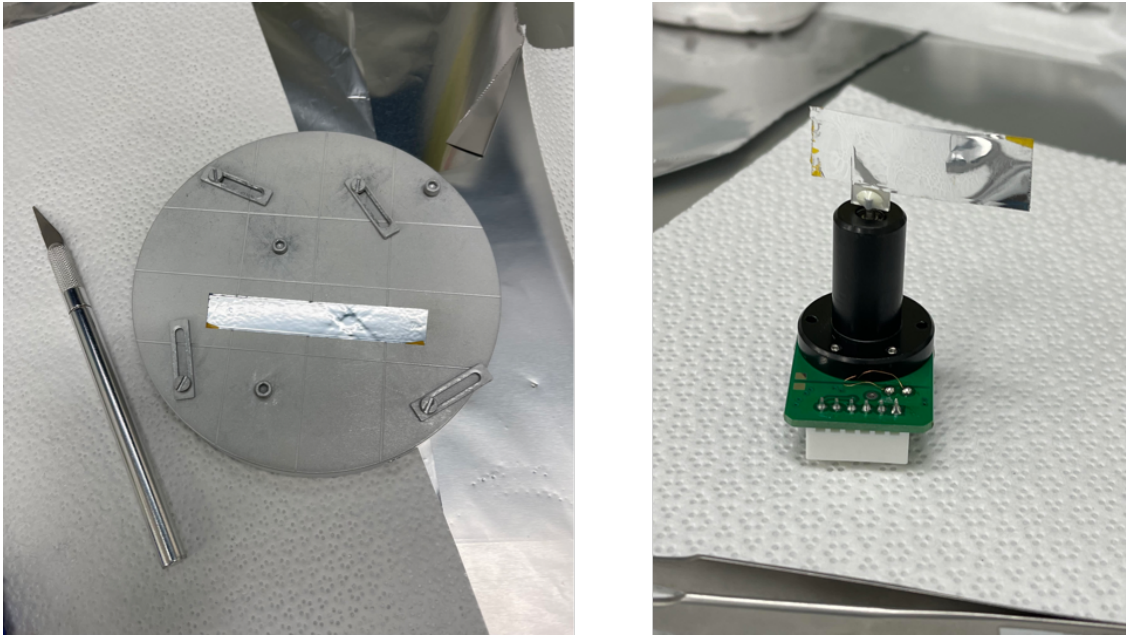
Figure 3.26: Left: kapton wire on the evaporator chuck, after the process was completed. Right: Galvo motor with kapton tape applied on the mirror.
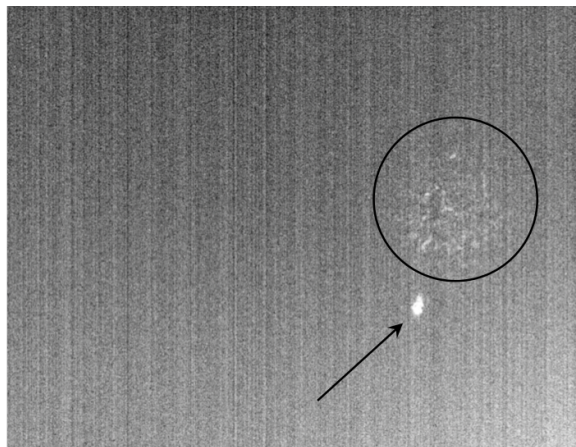
Figure 3.27: Deteriorated shape of the laser beam (pointed by the arrow), and stray reflections (circled in black.)

The gold mirrors were finally attached to the old mirrors of the galvo through a double-sided tape (the final result is shown in Fig. 3.28b). With this improved solution the mirror quality was drastically improved and the laser spot appeared perfectly round, and its intensity profile was the desired one (circular side lobes, like in Fig. 3.29).
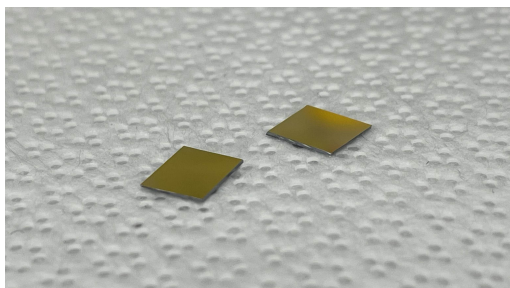
(a) Final result of the fabrication of the mirrors.
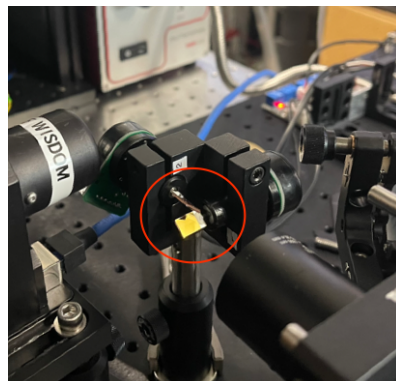
(b) Gold mirrors attached to the built-in galvo mirrors.

Figure 3.28: Final result of the fabrication of the gold mirrors.

Figure 3.29: This IR camera acquisition shows a round laser spot with circular lobes of the PSF[2].

Galvo motors signals

A modern mirror galvanometer works by utilizing a moving coil suspended in a stationary magnet's gap. A mirror attached to the coil reflects a beam of light, and as an electric current passes through the coil, it creates a magnetic field that interacts with the stationary magnet. This interaction causes the coil and attached mirror to rotate, deflecting the light beam. The deflection of the light beam is proportional to the current; from this it is intuitive to think that a larger voltage signal will produce a larger current in the coil, therefore inducing a larger deflection of the beam from the rest position. Therefore a naive approach to make the mirror oscillate would be applying square waves to the coils, at the frequency of interest. A better way to do it is by applying saw-tooth waves instead, in order to have a controlled and defined velocity of the mirrors and calibrate it according to the desired scan speed. After some experimentation, the signals that produce a scanning pattern with the desired FOV, are two saw-tooth waves with a 7V peak-to-peak amplitude, that are applied to the galvo controller board by a waveform

generator (Fig. 3.30). The frequency has been chosen to be low during the testing phase, to verify the correct behavior of the part.
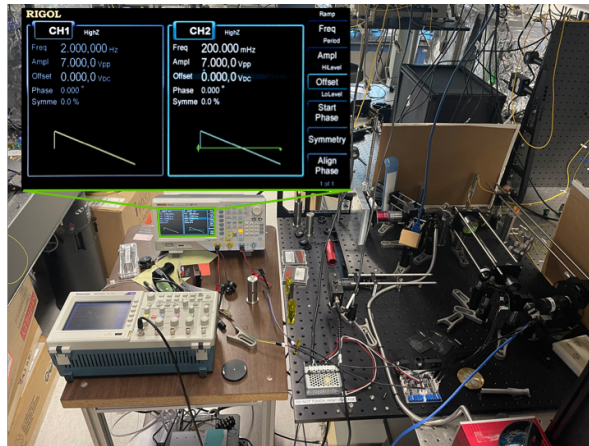
Figure 3.30: The galvo is controlled by a controller circuit board that allows separate control of the x and y motors. The power voltage is supplied by a DC-DC converter.

This part of the setup was also tested and produced satisfactory results: the function of scanning the sample was successfully achieved (Fig. 3.31).
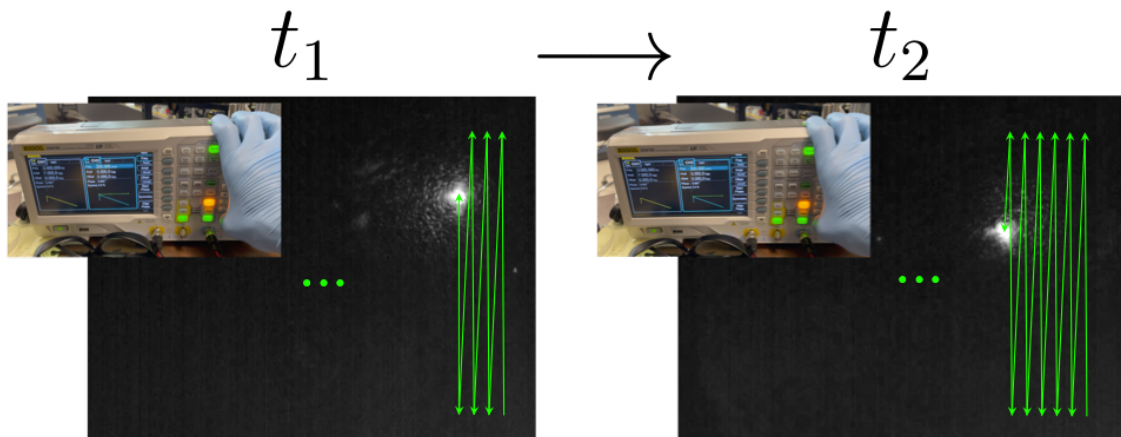
Figure 3.31: Representation of the raster scan performed by the system, with an optimal beam quality.

3.5   SHG path
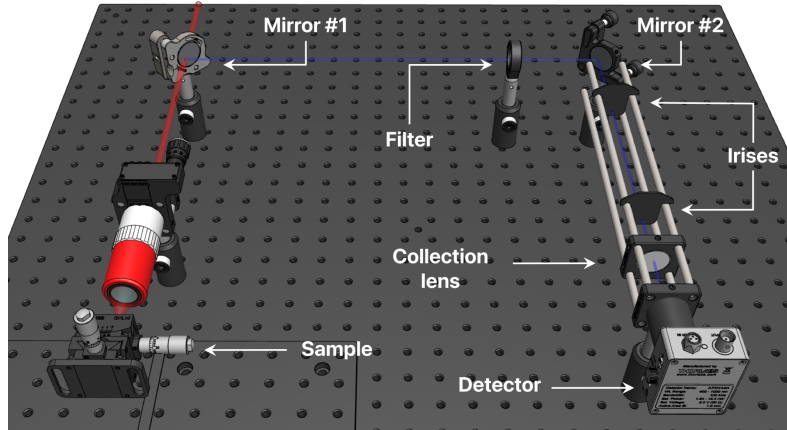
Figure 3.32: 3D representation of the SHG light path: the red laser beam represents the 1550 nm pump, the blue beam represents the 775 nm SHG light.

This part of the setup is composed of the components needed to direct the SHG light towards the detector, that is to say the dichroic mirror, an additional mirror to ease the alignment process (see Sec. B.1 for a more detailed explanation of this choice), the filter and a collection lens to focus the light on the APD. The SHG light produced by a 1550 nm laser will be at 775 nm, and therefore invisible to the naked eye; furthermore the expected power is well below what the human eye can see, even in the visible spectrum range. For this reason, a strategy relying on some other visible signal had to be employed.
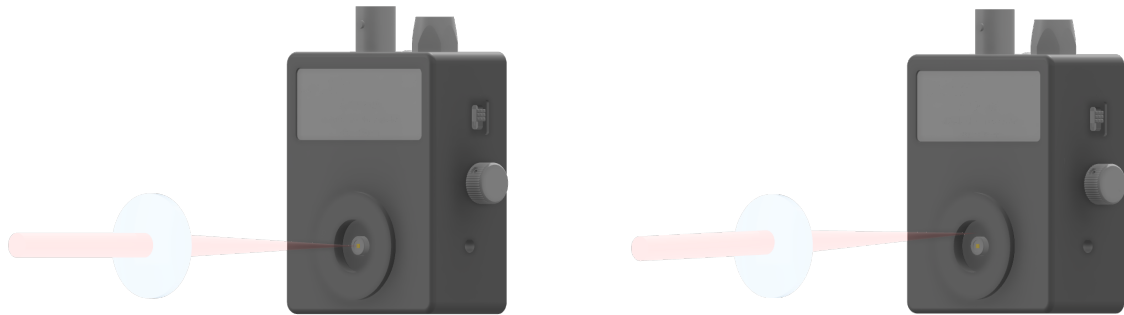
(a) The laser beam is perfectly aligned and the light gets focused on the photosensitive area of the detector.

(b) The angle is slightly off and the light gets focused on the detector body: small deflections of the beam will lead to no signal.

Moreover, this part of the setup required the finest alignment, because the detector area of the APD is extremely small (0.5 mm × 0.5 mm), therefore even a very small variation from the ideal angle (Fig. 3.33b) could provoke the light to be focused out of the detector area, therefore producing no signal. This was achieved in 3 steps, explained in the following paragraphs:

1. Preliminary alignment with visible red laser (Sec. 3.5.1)

2. Alignment with CMOS camera (Sec. 3.5.2)

3. Alignment with APD (Sec. 3.5.3)

3.5.1 Red laser alignment

This very first phase was useful to roughly decide where the APD would have been placed and perform a first alignment of the SHG path. This approach exploited a reverse procedure with respect to a standard alignment: a red fiber laser pen was coupled into free space through a collimator (Fig. 3.34a) that was mounted in substitution of the detector in Fig. 3.32. The 2 mirrors were then tilted in order to direct the light into the objective aperture (Fig. 3.34b).
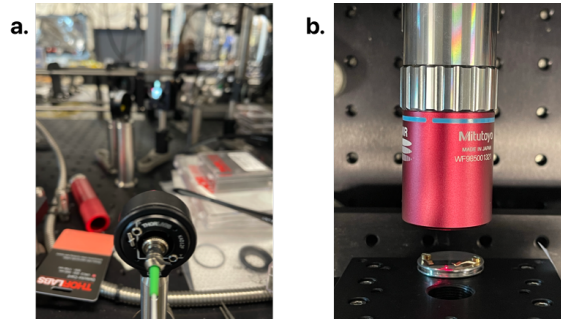
Figure 3.34: (a) The laser is shined at the second mirror so that the beam follows a path that is reversed with respect to the one SHG light is supposed to follow.
(b) The result of this process is the red light getting focused by the objective lens.

3.5.2 CMOS camera alignment

After this first procedure, which was useful to decide a position for the detector and to approximately align it to the path that the SHG would follow, a finer alignment procedure was needed. The idea behind this, is to exploit the previous results of the red laser alignment, and place a sensor with a big sensitive surface on the same optical post that was used to mount the red laser; this allowed having a big photosensitive area, roughly where the SHG signal was expected to be, in order to collect some of the non-perfectly-aligned light. The sensor of a CMOS camera was the easiest solution for this type of measurement. Nevertheless, the sensor is not sensitive in the SHG wavelength range, and the expected signal was too weak to be sensed by such a sensor. The problem was tackled by exploiting another form of visible light, given from a detector card, that was fixed on the sample holder (Fig. 3.35a). When the 1550 nm light is focused on the card, it fluoresces in the visible spectrum, and its intensity is high enough to be easily perceived with the naked eye and even more by a CMOS sensor. The fluorescence light is then collected by the objective lens and follows the same path that SHG light would follow, ending on the detector (or camera at this stage) post. The goal of this second

degree of alignment is to narrow down the area where the SHG signal was expected to be directed, preparing a spot where the APD would have been placed. In order to achieve such a goal, the camera was mounted in such a way that its center position would have been as close as possible to the one of the APD when mounted on the same support. A cage system was added too, in order to be able to mount a collection lens and freely change its distance from the detection point[8]. This light path was aligned following the principle described in B.1, using two cage-mountable irises to individuate the center of the camera (Fig. 3.35b).
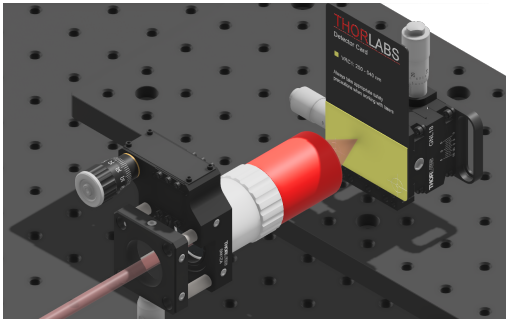
(a) The detector card was shined with the 1550 nm to cause fluorescence and use that signal for the alignment process.
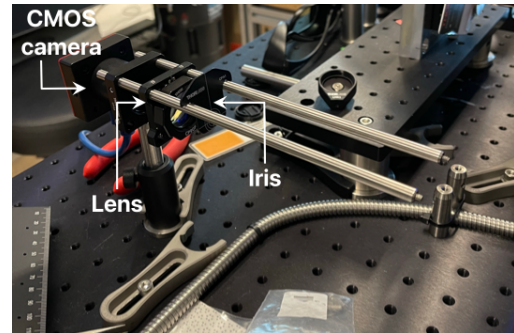
(b) Picture of the cage hosting the focusing lens, the camera, and the irises needed for the alignment (only one of the two is present in this photo). The configuration with both irises is depicted in Fig. 3.36a.

What could be seen from the camera is depicted in Fig. 3.36c. The same image observable by CMOS#1 is also captured by CMOS#2 and the purpose of this phase was to make the part of light responsible for the highest intensity part of the image, go through both the irises, so that it reaches the center of the camera sensor, with an angle as close as possible to 90°.

3.5.3 APD alignment

The third and final phase of the alignment consisted of substituting the CMOS camera with the detector that would have been used to measure SHG, the APD. The photodiode outputs a voltage that is proportional to the light intensity hitting it, this final phase was devoted to maximizing the output voltage by tuning:

- The focus

- Mirror#1

---

[8]The focusing lens has a certain working distance, i.e. the distance between the extremity of the lens and the point where light is properly focused. The APD and the camera, despite being mounted on the same support, will have their photosensitive elements at different depths inside their bodies. This means that the lens has to be moved when switching between the two components, to correctly focus the light.
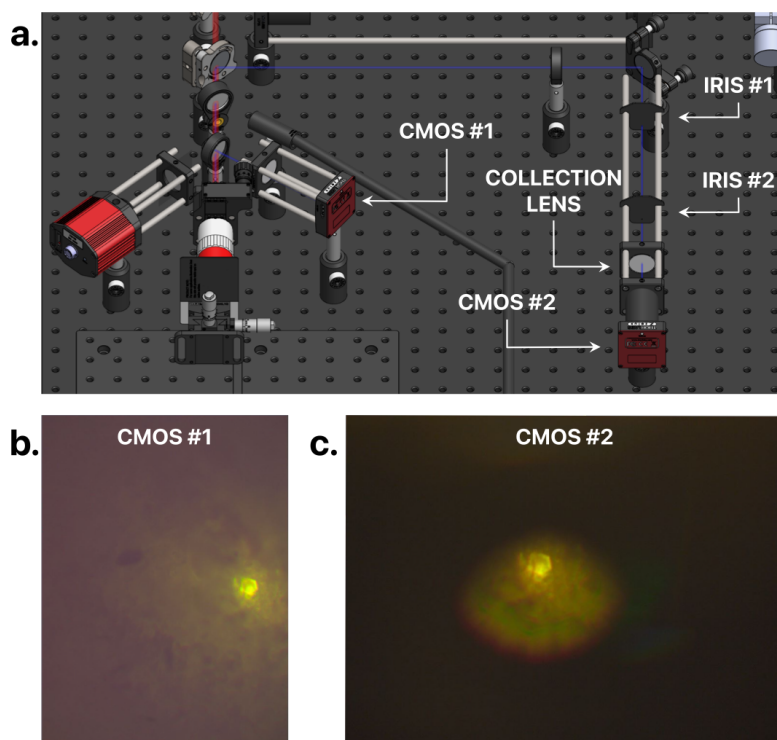
Figure 3.36: (a) The setup during the CMOS camera alignment.
(b) Image acquired by CMOS #1 (without irises).
(c) Image acquired by CMOS #2, simultaneous to image b (without irises).

- Mirror#2[9]

- Distance of the collection lens from the detector

This gave the maximum possible alignment for the measurement.

3.5.4 SHG measurement

After this long and precise procedure, the detector card was removed and the sample was mounted back on the sample holder; the LN chips were illuminated by the 1550 nm pulsed laser, producing short pulses of SHG light at 775 nm, but due to the detector limited bandwidth, they are smoothened and so the average powered is measured (as explained in Sec. 2.2, Fig. 2.13).

---

[9]The enumeration refers to Fig. 3.32.

Direct measurement

Initially, the measurements were performed in a direct mode: this means that the voltage output of the APD is directly used as a measurement. This first simple approach didn't lead to any results because the noise level was burying the signal of interest.

(a) Simple schematic representation of a direct type of measurement.

(b) In this case the signal is perturbed by the noise.
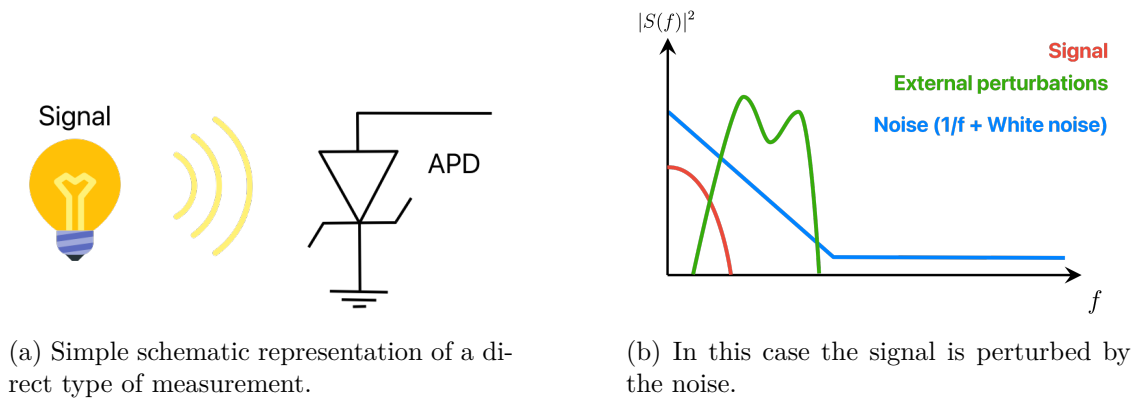
Figure 3.37: Direct detection mechanism.

Synchronous measurement (Lock-in)

A short explanation of synchronous measurement follows, to better explain how it is was used to avoid the noise problem.
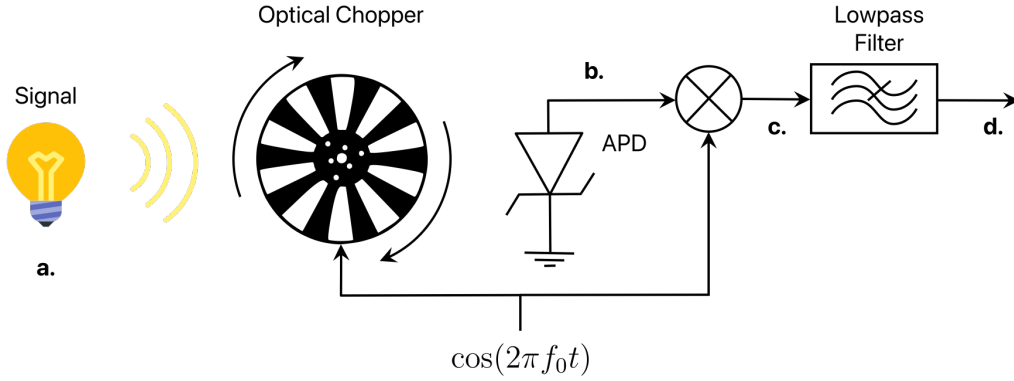
(a) Simple schematic representation of a synchronous type of measurement.
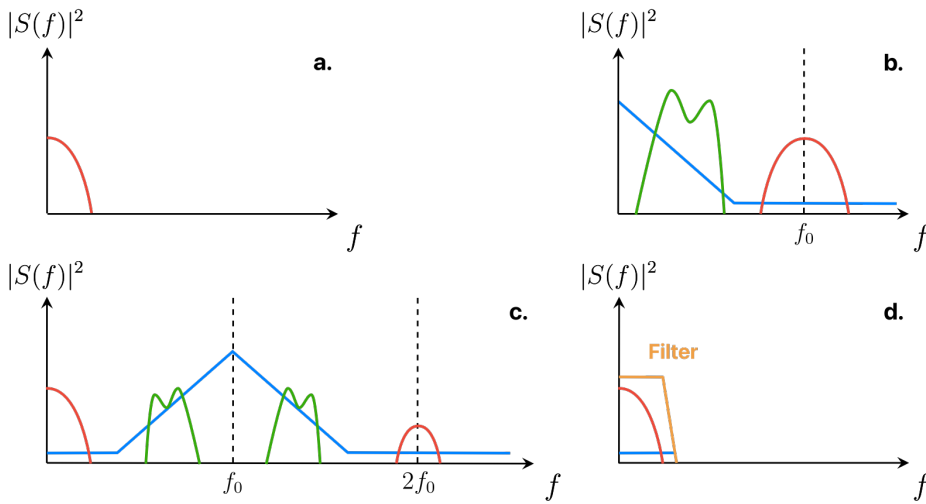
(b) In this case the noise does not affect the signal as much.

Figure 3.38: Synchronous detection mechanism.

Figure 3.38a illustrates how the experimental setup was modified to accommodate this methodology. An optical chopper is inserted between the signal path and the detector[10]. Effectively, this action implies modulating the signal, shifting its spectrum around the

---

[10]In our case, for the sake of simplicity, the chopper was placed between the source and the sample: this results in the chopped modulation of the SHG signal as well, since it is generated only when the primary source interacts with the sample.

frequency f_0, which corresponds to the rotational frequency of the chopper. It is at this node that noise sources are incorporated into the signal. However, the overlap does not pose a problem, given that the $1/f$ noise is considerably reduced at f_0, and external sources typically are at lower frequencies; the remaining noise component is only white noise. Subsequently, the signal is further shifted by f_0 to the right, and a low-pass filter is employed to eliminate everything except the signal of interest.

SHG measurement

The measurement presented in this section was obtained using the alignment procedures specified in the previous sections, and a synchronous detection principle with a lock-in amplifier (SR830). SR830 is responsible for the signal processing operations from point b. to point d. (in Fig. 3.38), and the related settings can be tuned in order to obtain the best measurement. The parameters that most heavily affect the measurement are highlighted with a red shape in Fig. 3.39; the time constant (which dictates how fast the output signal can vary in time) was set to 300 ms (a.), the sensitivity to 100 mV (b.) and the modulation frequency was set by an external signal coming from the optical chopper rotating at 365 Hz (c.). The final measurement of the signal with the following configuration and all the previous considerations led to a measured SHG signal of around 26 mV on the lock-in amplifier, which corresponds to 26 mV $\times\sqrt{2}$ mV $\sim$ 36 mV on the APD, i.e. a power of 13.3 pW (see Sec. 2.2 for details about APD440A relation between measured power and output voltage), that is higher than the expected one, most likely because of the approximations involved in the calculations. To make sure the

Figure 3.39: SR830 interface. Image taken from Stanford Research Systems.

measured signal was actually SH light and not some other disturbance, it was filtered with an additional FELH0600 longpass filter with a 600 nm cut-on wavelength, in order to restrict the range of wavelengths to a narrower interval. The measured signal resulted intact after this modification; subsequently, a FESH0450 shortpass filter with a 700 nm cut-off wavelength was applied and the signal disappeared, suggesting that the signal is SHG.

61

Chapter 4

Conclusion

This work explains the basic physics behind SHG microscopy and highlights all the most critical considerations and design aspects that have a central role in this project and similar ones. The technical aspects of the optical system are explored in depth, as they guided the design of the instrument and were fundamental to achieving the desired performances. The structure of the instrument was divided into 4 fundamental blocks that are well explained in the body of this thesis: the fiber-free space coupling section provides a complete explanation of pulse broadening in optical fibers, which is essential to estimate the peak power decrease. The 4f-like system section explains the most important aspects of a laser scanning system and suggests numerous solutions to problems that may occur during the implementation of these systems. The section about wide-field imaging is helpful for building a traditional microscope and the final section about the SHG path offers a wide selection of alignment methods for different situations. The instrument was built and is completely functional, the laser beam is correctly managed and transported to the sample; the scanning mechanism is effectively providing a satisfactory FOV over the samples and the SH light was generated and measured in several experiments. Nonetheless, this does not mean that the project can't be continued: the next and final step will involve coordinating all the components through a centralized MATLAB code to reconstruct the images starting from the point-by-point information given by the SHG signal. The particular configuration of the setup, together with the code reconstructing the images, will allow the retrieval of precious information about the poling depth while performing the poling process; this will allow the optimization of the parameters involved in the operation, possibly through machine learning algorithms that run independently while the sample is being observed through the microscope.

4.1 Further improvement of phase matching: micro-heaters

The main goal of this thesis was to develop an instrument able to analyze the SHG signal coming from the chips to retrieve information about the poling depth and consequently improve the poling process. Nevertheless, some aspects cannot be addressed through the optimization of the poling process itself. One example is the dependence on fabrication, which is discussed in the next section.

4.1.1 Working principle

As discussed in Chap. 1, periodic poling is an efficient way of achieving QPM, and one can compensate for the momentum mismatch $\Delta k = k_{2\omega} - 2k_\omega = \frac{4\pi}{\lambda}\left(n_{2w} - n_w\right)$ by setting a Λ, where $2\pi/\Lambda = \Delta k$ (see Sec. 1.2.1). In waveguides the mismatch is given by $\Delta k = \frac{4\pi}{\lambda}\left(n_{2w}^{\text{eff}} - n_w^{\text{eff}}\right)$, where n^{eff} is the effective index of the mode propagating in the waveguide and quantifies the phase change per unit length, just like the refractive index does in bulk materials. The effective index depends on both the material refractive index and the waveguide geometry, which is subject to the uncertainties introduced by the fabrication processes. Therefore, these errors will alter the waveguide's effective index and the QPM condition. To compensate for the disorder, one can change the temperature of the waveguide in order to modify the material refractive index and cancel out the detrimental effect of the fabrication[1].

4.1.2 COMSOL simulations

The structure was simulated in COMSOL®: the main goal was to find the optimal distance between the heaters and the waveguide to induce a 100 K temperature difference at the center of the latter (which is the target temperature to make up the effective index change). The other parameters were fixed from the geometry of the actual device on which the microheaters were applied. The stack is the following (from bottom to top):

- SiO_2 substrate

- LN rib waveguide: 200 nm (bottom layer) + 300 nm (top layer)

- SiO_2 cladding: 700 nm

- Ti heaters: 200 nm

- Top SiO_2 insulating layer: 700 nm

- Air

After some parametric simulations using the "Heat transfer in Solids and Fluids[2]" interface, the optimal distance was found to be 2.1 μm; the temperature behavior is reported in Fig. 4.2.

---

[1] Alternative solutions were explored by other people, like in [4].

[2] The fluids interface was useful to account for the convection in air.
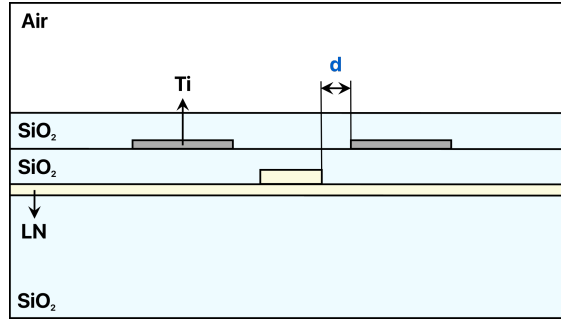
Figure 4.1: LN waveguide stack. d is the distance that was optimized.
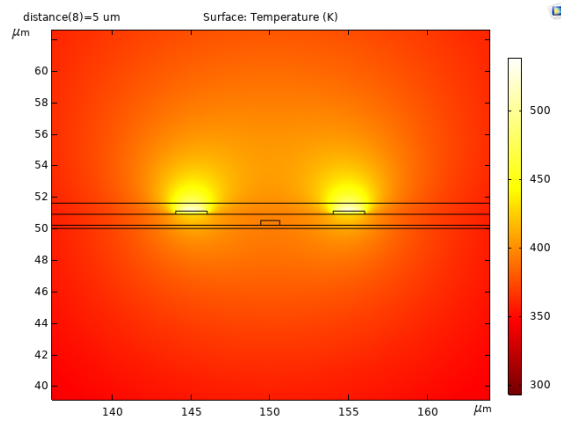
Figure 4.2: 2D temperature distribution over the cross-section of the structure. The temperature in the central point of the waveguide is expected to be 393 K.

4.1.3 Layout

After the simulations, the structure was replicated in a layout, to pattern the heaters on a real chip, consisting of 8 different devices. This allowed sweeping the distance around the optimal one of 2.1 μm, for 8 different values (Fig. 4.3).

In order to simultaneously actuate all 7 heaters on each waveguide, they will be actuated by a 14-needle (1 signal needle and 1 GND needle), 7-channel probe. In order to allow this kind of actuation, pads and routing wires have been added to the layout (Fig. 4.4).

(a) Layout of the heaters, without routing wires.
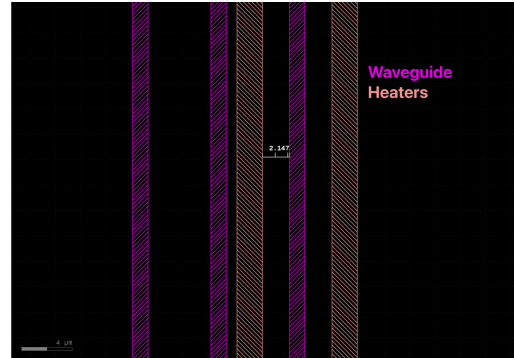
(b) Zoomed view of the heaters. The distance between them and the waveguide is 2.147 μm.

Figure 4.3: Heaters layout.
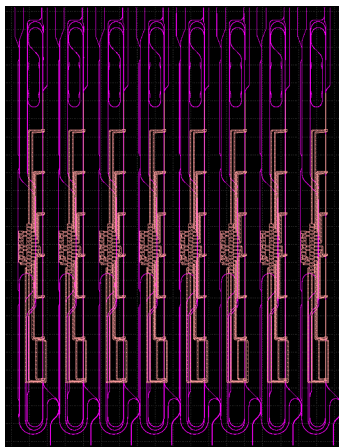
(a) Layout of the heaters, with the routing wires.
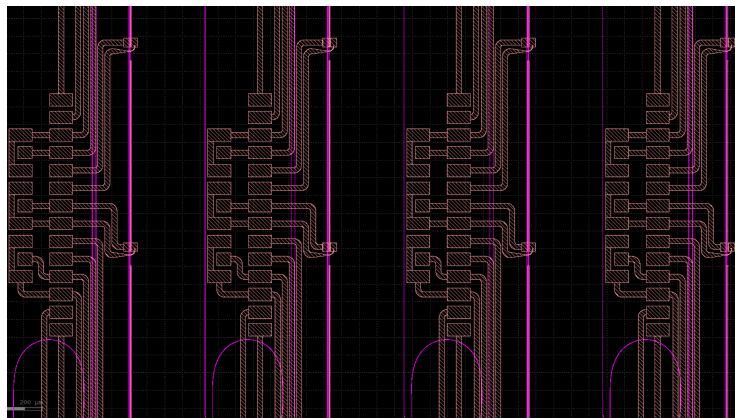
(b) Zoomed view.

Figure 4.4: Heaters layout with the routing wires. Note that the wires are much wider than the heaters to have most of the voltage drop across the heaters, which will have a higher resistance. To prevent losses, their width decreases on the trait overlapping with the waveguide. The nine pads on the left are there to make the design compatible with an old probe (GSG, three channels).

4.1.4 Fabricated structure

The heaters layer was then fabricated in the cleanroom; the structure was patterned through lift-off, and some images acquired through a microscope are reported in Fig. 4.5.
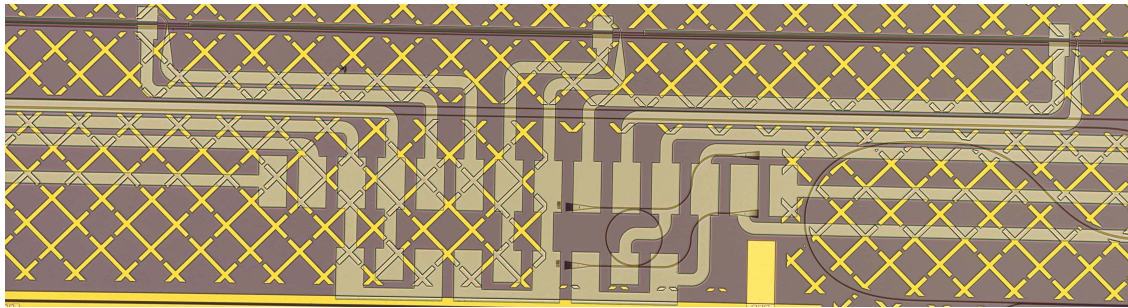
(a) Post Ti deposition image of the heaters.
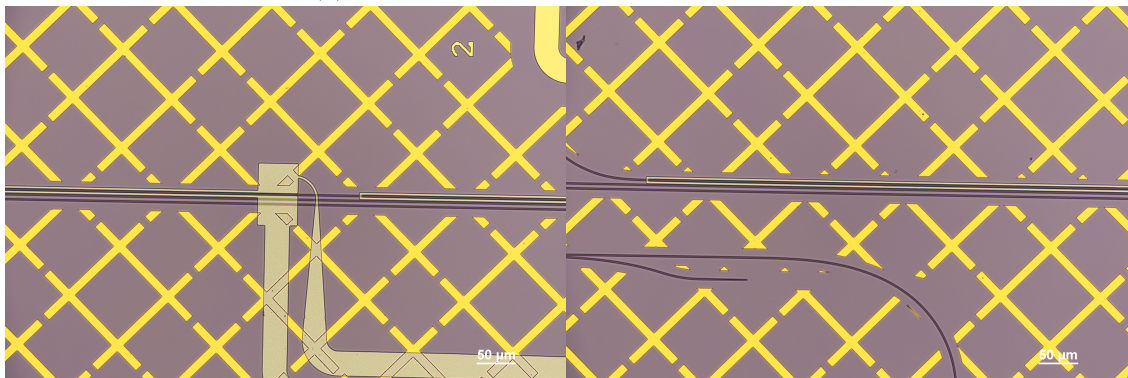
(b) Zoomed view on the initial part of the heater. (c) Zoomed view on the final part of the heater.
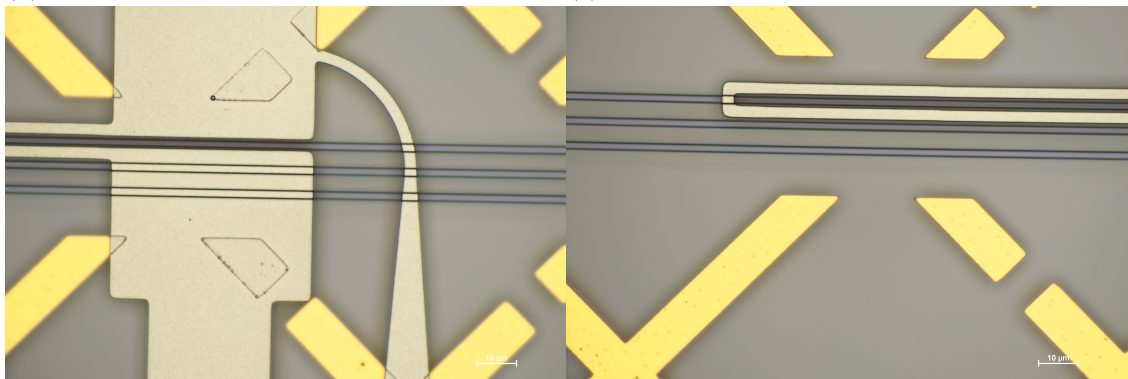
(d) Closer zoomed view on the initial part of the (e) Closer zoomed view on the final part of the heater. heater.

Figure 4.5: Microscope acquisitions of the heaters.

67

4.1.5   Future prospects of this project

This project is still to be completed and the future steps will be contacting the pads with the probe and lead measurements on the waveguides, to assess the correct behavior of the micro-heater devices.

Appendix A

MATLAB code

This annex contains MATLAB code that was used for various purposes.

A.1   SHG power estimation

Listing A.1: SHG calculation.

```matlab
clear all
close all
clc

% useful parameters
lambda = 1550e-9;
eps_0 = 8.85e-12;
n_BOX_2w = 1.4538;
n_LN_2w = 2.26;
n_Si_2w = 3.7139;
% detector_responsivity = 58e-3; % [A/W]



% Input variables
T = 1/80e6;             % Repetition period [s]
P_avg = 10e-3;          % average power [W]
tau_p = 1200e-15;        % pulse duration [s]

% Compute P_peak
P_peak = P_avg * T / abs(tau_p) * sqrt(2/pi);


T_galvo = 0.981;
T_scan = 0.93;
T_tube = 0.87;
T_dichroic = 0.98;
```

```matlab
T_obj = 1;

P_w = P_peak*(T_galvo)^2*T_scan*T_tube*T_dichroic*T_obj

% Define the variables and parameters
chi_2 = 34e-12;      % Nonlinear susceptibility
A = pi*((500e-9)^2);          % Cross-sectional area (in m^2)
c = 299792458;                % Speed of light (in m/s)
w = 2*pi/lambda;          % Frequency of the light wave (in
   1/m)
eps_w = (2.2111^2);           % Dielectric constant at
   frequency w
eps_2w = (2.26^2);            % Dielectric constant at
   frequency 2w
Delta_k = 4*pi/lambda*(sqrt(eps_2w) - sqrt(eps_w));   % Phase
   mismatch (in m^-1)
L = 500e-9;                   % Interaction length (in m)

% Calculate P_2w
P_2w = chi_2*((P_w^2)/(A))*L^2*((32*pi^3*w^3)/(c^3*eps_w*sqrt
   (eps_2w)));

% Define interafaces R

R_LN_BOX = abs((n_LN_2w - n_BOX_2w)/(n_LN_2w + n_BOX_2w))^2;
R_BOX_Si = abs((n_BOX_2w - n_Si_2w)/(n_BOX_2w + n_Si_2w))^2;

P_objective = P_2w * (1 - R_LN_BOX) * R_BOX_Si * (1 -
   R_LN_BOX);


% Define transmissions
T_obj_2w = 1;
R_dichroic_2w = 0.995;
T_filter_2w = 0.982;
T_collection_2w = 1;

% Calculate P_detector
P_detector = P_2w*T_obj_2w*R_dichroic_2w*T_filter_2w*
   T_collection_2w
P_avg_detector = P_detector*tau_p/T*sqrt(pi/2)
% det_voltage = P_avg_detector*3e6*55e-3*11e3 % PMT thesis
det_voltage = P_avg_detector*54*50e6 % APD440A
```

A.2 Resolution computation without paraxial approximation

Listing A.2: A GUI MATLAB script useful to make considerations about the resolution and make design choices regarding that matter.

```matlab
function sliderGUI
clear all
close all
clc

% Create the main figure
fig = figure('Name', 'NA and w_{xy} Slider', 'NumberTitle', 'off', ...
             'Position', [100, 100, 800, 500]);

% Parameters
lambda_options = [1e-6, 1550e-9];
lambda = lambda_options(1);
NA_min = 0.01;
NA_max = 1.5;

% Initial NA value
NA_init = 0.5;

% Calculate initial w_xy value
w_xy_init = w_xy_calc(NA_init, lambda);

% Create the slider
slider = uicontrol('Parent', fig, 'Style', 'slider', ...
                   'Position', [100, 80, 400, 20], ...
                   'value', NA_init, 'min', NA_min, ...
                   'max', NA_max, 'Callback', @
                       slider_callback);

na_textbox = uicontrol('Parent', fig, 'Style', 'edit', ...
                   'Position', [480, 80, 80, 20], ...
                   'String', num2str(NA_init), ...
                   'Callback', @na_textbox_callback);


% Create the text box
textbox = uicontrol('Parent', fig, 'Style', 'edit', ...
                   'Position', [580, 80, 80, 20], ...
                   'String', num2str(w_xy_init));
```

```matlab
% Create the dropdown menu
dropdown = uicontrol('Parent', fig, 'Style', 'popupmenu',
    ...
                        'Position', [100, 140, 100, 20], ...
                        'String', {'1e-6', '1550e-9'}, ...
                        'Callback', @dropdown_callback);

% Create labels
uicontrol('Parent', fig, 'Style', 'text', ...
            'Position', [100, 50, 100, 20], ...
            'String', 'NA Slider');

uicontrol('Parent', fig, 'Style', 'text', ...
            'Position', [580, 50, 100, 20], ...
            'String', 'w_{xy}');

uicontrol('Parent', fig, 'Style', 'text', ...
            'Position', [100, 110, 100, 20], ...
            'String', 'Lambda');

% Create axes for the plot
ax = axes('Parent', fig, 'Position', [0.25, 0.4, 0.5,
    0.5]);

% Initial plot
update_plot(NA_init);

% Slider callback function
function slider_callback(source, ~)
    % Get the current NA value from the slider
    NA = source.Value;

    % Calculate the w_xy value for the current NA
    w_xy = w_xy_calc(NA, lambda);

    % Update the text boxes with the new NA and w_xy
        values
    na_textbox.String = num2str(NA); % <-- Add this line
    textbox.String = num2str(w_xy);

    % Update the plot
    update_plot(NA);
end
```

```matlab
% Dropdown callback function
function dropdown_callback(source, ~)
    % Get the selected lambda value
    lambda = lambda_options(source.Value);

    % Update the w_xy value for the new lambda
    NA = slider.Value;
    w_xy = w_xy_calc(NA, lambda);

    % Update the text box with the new w_xy value
    textbox.String = num2str(w_xy);

    % Update the plot
    update_plot(NA);
end

% Function to calculate w_xy
function w_xy = w_xy_calc(NA, lambda)
    if NA <= 0.7
        w_xy = 0.32 * lambda / (sqrt(2) * NA);
    else
        w_xy = 0.325 * lambda / (sqrt(2) * NA^0.91);
    end
end

% Function to update the plot
function update_plot(NA_current)
    % Calculate w_xy values for the plot
    NA_plot = linspace(NA_min, NA_max, 1000);
    w_xy_plot = arrayfun(@(NA) w_xy_calc(NA, lambda), ...
        NA_plot);

    % Clear the current plot and plot the new data
    cla(ax);
    plot(ax, NA_plot, w_xy_plot);
    xlabel(ax, 'NA');
    ylabel(ax, 'w_{xy}');
    title(ax, 'Plot of w_{xy} function');
    grid(ax, 'on');

    % Add a vertical line at the current NA value
    w_xy_current = w_xy_calc(NA_current, lambda);
    hold(ax, 'on');
```

```matlab
            plot(ax, [NA_current, NA_current], [min(w_xy_plot),
                w_xy_current], '--r');
            hold(ax, 'off');
    end

    function na_textbox_callback(source, ~)
        % Get the updated NA value from the textbox
        NA = str2double(source.String);

        % Check if the NA value is within the valid range
        if NA < NA_min || NA > NA_max
            % Display a warning message and revert to the
                previous slider value
            warndlg('Invalid NA value. Please enter a value
                within the slider range.');
            source.String = num2str(slider.Value);
            return;
        end

        % Update the slider value
        slider.Value = NA;

        % Calculate the w_xy value for the updated NA
        w_xy = w_xy_calc(NA, lambda);

        % Update the w_xy textbox
        textbox.String = num2str(w_xy);

        % Update the plot
        update_plot(NA);
    end

end
```

Appendix B

Additional explanatory material

This section contains paragraphs that could be useful for the reader to get familiar with the topics and techniques utilized in this thesis that didn't find a proper place in the document's main body.

B.1 Beam-walking

Beam walking is a technique commonly used in photonics to align a laser beam along a desired path by means of two mirrors and two irises. It was the technique used for all the alignment procedures in this work and therefore this paragraph will be devoted to explaining its operation.
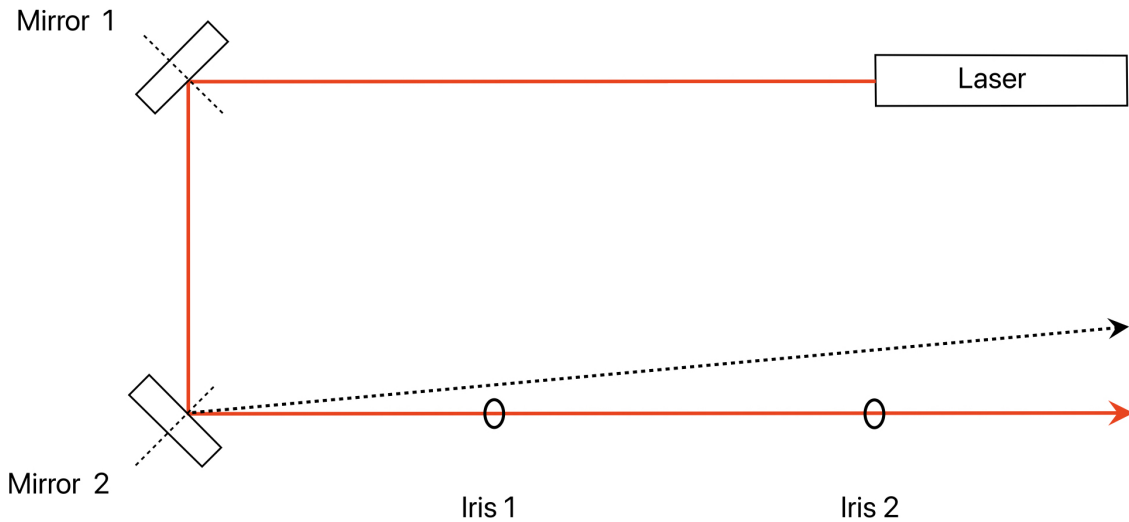
Figure B.1: Beam-walking technique illustration; the second mirror can be positioned at a 90° clockwise angle to maintain the same propagation direction.

The desired path will be defined by the two irises' apertures, as the line that passes through both of them. Once the two irises have been placed, the first mirror can be placed such that the beam is reflected and it does a 90° angle with respect to its initial

direction. The second mirror can now be placed as to intercept the new beam path and deflect it with a further 90° angle. During this phase, the mirror adjusters should be as close as possible to the middle of their range in order to be able to provide the largest correction possible in all directions without being moved. After that the first mirror will be regulated so as to make the beam pass through the first iris; at this point the second mirror serves as a second degree of freedom to make the beam passing through the first iris, hit the center of the second iris. This is usually not achievable after the first deflection of the first mirror, as deflecting the beam with the second mirror during this phase will most likely cause the light to be blocked by the first iris. This is why this process is iterative, and one has to continuously alternate the deflection of the first and second mirrors until the beam can pass through both the irises.

Appendix C

Costs

C.1   Table of purchased components

Product	PART NO.	No.	Lead time	Unit Price	Subtotal
Collimator	F230APC-1550	1	-	$240.45	$240.45
Scan lens	SL50-3P	1	-	$4'700.45	$4'700.45
Tube lens	TL200-3P	1	-	$6'091.02	$6'091.02
Dichroic Mirror	DMLP950T	1	-	$202.64	$202.64
Dry Objective	MY50X-825	1	-	$4'511.75	$4'511.75
Mirror mount	POLARIS-K1E3	3	-	$165.90	$497.70
Dichroic mirror (EO)	Dichroic Longpass Filter	1	-	$165.00	$165.00
Hex adjusters	HKTS-5/64	2	-	$27.86	$55.72
1 mm spacers	RS1M	10	-	$7.51	$75.10
9 mm spacers	RS9M	10	-	$9.73	$97.30
Total:					**$16'942.93**

Table C.1: Purchased components.

Bibliography

[1] *Nonlinear Optics*. Elsevier, 2003.

[2] Govind Agrawal. Group-velocity dispersion. In *Nonlinear Fiber Optics*, pages 57–85. Elsevier, 2013.

[3] Gerhard Berth, Volker Wiedemeier, Klaus-Peter HÃ¼sch, Li Gui, Hui Hu, Wolfgang Sohler, and Artur Zrenner. Imaging of ferroelectric micro-domains in x-cut lithium niobate by confocal second harmonic microscopy. *Ferroelectrics*, 389(1):132–141, oct 2009.

[4] Pao-Kang Chen, Ian Briggs, Chaohan Cui, Liang Zhang, Manav Shah, and Linran Fan. Adapted poling to break the nonlinear efficiency limit in nanophotonic lithium niobate waveguides. *arXiv preprint arXiv:2307.11671*, 2023.

[5] Xin Chen, Wieslaw Krolikowski, and Yan Sheng. Nonlinear optical effects at ferroelectric domain walls. In *Ferroelectrics and Their Applications*. InTech, October 2018.

[6] R. Gauderon, P.B. Lukins, and C.J.R. Sheppard. Optimization of second-harmonic generation microscopy. *Micron*, 32(7):691–700, oct 2001.

[7] Bastian Knabe, Karsten Buse, Wilfried Assenmacher, and Werner Mader. Spontaneous polarization in ultrasmall lithium niobate nanocrystals revealed by second harmonic generation. *Physical Review B*, 86(19), nov 2012.

[8] Juanjuan Lu, Joshua B. Surya, Xianwen Liu, Alexander W. Bruch, Zheng Gong, Yuntao Xu, and Hong X. Tang. Periodically poled thin-film lithium niobate microring resonators with a second-harmonic generation efficiency of 250,000%/w. *Optica*, 6(12):1455, nov 2019.

[9] Timothy P. McKenna, Hubert S. Stokowski, Vahid Ansari, Jatadhari Mishra, Marc Jankowski, Christopher J. Sarabalis, Jason F. Herrmann, Carsten Langrock, Martin M. Fejer, and Amir H. Safavi-Naeini. Ultra-low-power second-order nonlinear optics on a chip. *Nature Communications*, 13(1), August 2022.

[10] M. Rüsing, J. Zhao, and S. Mookherjea. Second harmonic microscopy of poled x-cut thin film lithium niobate: Understanding the contrast mechanism. *Journal of Applied Physics*, 126(11), September 2019.

[11] Chris Velzel. *A Course in Lens Design*. Springer Netherlands, 2014.

[12] Wikipedia contributors. Parseval's theorem. https://en.wikipedia.org/wiki/Parseval%27s_theorem, March 2023.

[13] Michael D. Young, Jeffrey J. Field, Kraig E. Sheetz, Randy A. Bartels, and Jeff Squier. A pragmatic guide to multiphoton microscope design. *Advances in Optics and Photonics*, 7(2):276, June 2015.

[14] Jie Zhao, Michael Rüsing, Usman A. Javid, Jingwei Ling, Mingxiao Li, Qiang Lin, and Shayan Mookherjea. Shallow-etched thin-film lithium niobate waveguides for highly-efficient second-harmonic generation. *Optics Express*, 28(13):19669, jun 2020.

List of Figures